JM PAPERS

A continuum model of discrete granular avalanches

Min-Chi Liang[1] and Hervé Capart [1],†

[1]Department of Civil Engineering and Hydrotech Research Institute, National Taiwan University, Taipei 106, Taiwan

A simple continuum model is proposed for discrete granular avalanches, as observed in slowly rotating drums. Subject to granular transfer across the basal interface, the model evolves the transient surface inclination and mid-slope velocity profile of the avalanches, from failure to arrest. This is done using new boundary conditions that allow entrainment or detrainment contingent on the basal shear rate. For entrainment to occur, the basal shear stress must overcome the erosion resistance of the jammed deposit, while for detrainment to take place the basal shear rate must vanish. The resulting avalanche dynamics is controlled by a single dimensionless number, the ratio of excess slope at failure to excess resistance to erosion, that can be determined from inclination history data. This number provides a measure of slope brittleness, from which the peak flow rate and arrest inclination can be predicted. Analytical techniques are used to derive model solutions, and clarify the resulting behaviour. Finally, the model is tested by comparing solutions with laboratory experiments and discrete particle simulations.

Key words: avalanches, dry granular material

1. Introduction

Based upon rheological descriptions of granular behaviour (Silbert *et al.* 2001; da Cruz *et al.* 2005; Jop, Forterre & Pouliquen 2006), continuum models have in recent decades been applied successfully to a variety of granular surface flows. These include flows over rigid boundaries (Edwards *et al.* 2019; Lin & Yang 2020) and flows over erodible layers. The latter include steady channel flows (Jop, Forterre & Pouliquen 2005; Liu & Henann 2017; Berzi, Jenkins & Richard 2020), transient channel flows (Jop, Forterre & Pouliquen 2007; Capart, Hung & Stark 2015; Parez, Aharonov & Toussaint 2016; Larcher, Prati

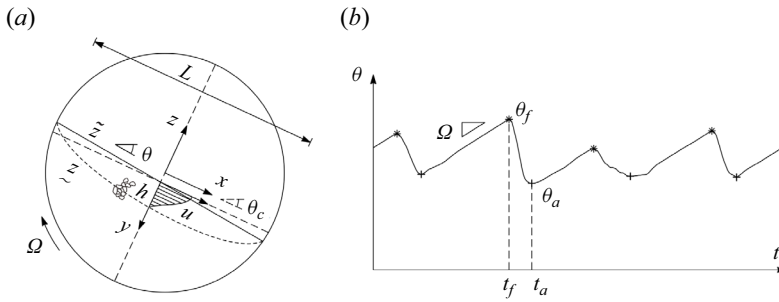† Email address for correspondence: hcapart@yahoo.com

Figure 1. Discrete avalanches in a slowly rotated drum: (*a*) definition sketch with key parameters and variables; (*b*) typical surface inclination history, featuring a series of sudden slope relaxation events lasting from failure at time t_f to arrest at time t_a.

& Fraccarollo 2018; Capart 2023) and steady, continuous avalanching in rotating drums and draining silos (Hung, Stark & Capart 2016; Hung, Aussillous & Capart 2018; Hung *et al.* 2023). Important flows over erodible beds that have so far resisted this approach, however, are the discrete avalanches produced in very slowly rotated drums (Evesque 1991; Courrech du Pont *et al.* 2005; Liu, Zhou & Specht 2010; Balmforth & McElwaine 2018), in gradually tilted sand boxes (Jaeger, Liu & Nagel 1989; Evesque *et al.* 1993; Aguirre *et al.* 2000) or down continuously supplied sand piles (Lemieux & Durian 2000; Altshuler *et al.* 2008; Arran & Vriend 2018; Alonso-Llanes *et al.* 2022). In such configurations, granular slopes can remain at rest in a metastable state, then suddenly relax to milder inclinations by way of short-lived surface avalanches. In slowly driven experiments that used ionic concentration to turn interparticle friction on and off, Perrin *et al.* (2019) found that sawtooth-shaped hysteretic avalanches occurred for frictional particles, but that hysteresis completely disappeared for frictionless particles.

In rotating drums, the regime in which discrete avalanches occur is known as the slumping regime, as opposed to the rolling and cascading regimes for which grains flow continuously and steadily along the surface. As illustrated by figure 1(*a*), a characteristic of the slumping regime is that the granular free surface remains nearly straight as it evolves over time. For the rolling regime, the surface is also nearly straight, but maintains a steady inclination, whereas for the cascading regime the steady free surface becomes curved (Rajchenbach 1990; Hung *et al.* 2016; Li & Andrade 2020). In the slumping regime, observed at very slow rotation rates, avalanches occur episodically, alternating with periods of pure rigid body rotation. As illustrated by figure 1(*b*), during these periods the surface inclination gradually steepens, before the next avalanche occurs. During each avalanche, grains typically accelerate from rest, then decelerate back to arrest within a short time. Granular motion is often limited to a surface layer, but the thickness of this layer can grow and decay over time as the avalanche entrains and detrains grains at the base. The basal boundary is therefore a moving non-material interface (Jop *et al.* 2007; Lusso *et al.* 2021; Capart 2023). As for other geomorphic flows (Hungr 1995), bulking and debulking may significantly affect the flow dynamics, and in particular control the peak flow rate. Unlike most geomorphic flows, however, water is not needed. Instead, the flowing layer and static deposit are composed of the same material: dry grains.

In nature, episodic avalanches of dry grains can be observed down screes or debris slopes (Church, Stock & Ryder 1979; Dai *et al.* 2022), or down the lee faces of eolian dunes (Allen 1970; Sherman *et al.* 2022). Related phenomena, also involving the failure of metastable slopes, include landslides and snow avalanches. The study of rotating drum

avalanches can thus help clarify generic features of granular flows that are of much broader interest (Evesque 1991; Linz, Hager & Hänggi 1999; Perrin *et al.* 2019). In particular, episodic avalanches of dry grains represent possibly the simplest case in which a small perturbation, slow steepening or gradual weakening can produce a disproportionate slope response. The prediction of the resulting amplitude, peak flow rate and eventual arrest inclination is therefore a problem of practical as well as fundamental interest.

To simulate the dynamics of discrete avalanches, a number of phenomenological models have been proposed and applied to rotating drum flows (Bouchaud *et al.* 1994; Linz *et al.* 1999; Fischer *et al.* 2008; Fischer, Gondret & Rabaud 2009; Marteau & Andrade 2018). Typically, these models formulate an ordinary differential equation for the time-evolving surface inclination $\theta(t)$ (see figure 1*a*,*b*), with terms designed to replicate experimentally observed behaviours. Although such models provide valuable insights, they do not deduce the flow dynamics from generally applicable, explicit assumptions about local granular behaviour. Continuum models, on the other hand, have been successful at describing avalanching flows released from rest by suddenly lifting a lid (Jop *et al.* 2007; Larcher *et al.* 2018) or tilting a channel (Capart *et al.* 2015). These include models resolved over the vertical (Jop *et al.* 2007; Sarno *et al.* 2022), or integrated over depth (Capart *et al.* 2015). So far, however, no continuum model has been able to evolve the inclination and velocity profile of self-triggered avalanches like those observed in slowly rotating drums.

In the present work, we propose such a deductive model, based on two essential components. The first is a local flow rheology, provided by the linearized $\mu(I)$ model relating the stress ratio μ to the inertia number I (da Cruz *et al.* 2005; Jop *et al.* 2006). The second is a new set of basal boundary conditions, proposed recently for granular flows over brittle erodible beds (Capart 2023). These assert that, for entrainment to occur, the basal shear stress must overcome the erosion resistance of the jammed deposit, while for detrainment to take place the basal shear rate must vanish. Bypass takes place when neither entrainment or detrainment can occur. The adopted rheology, although simple, is supported by experiments (Jop *et al.* 2005; Tapia, Pouliquen & Guazzelli 2019) and discrete particle simulations (da Cruz *et al.* 2005; Azéma & Radjaï 2014). The basal boundary conditions, by contrast, have so far been confronted only with experiments involving starting and stopping flows, down slopes of constant inclination (Capart *et al.* 2015; Larcher *et al.* 2018). Their application to episodic avalanches, down slopes of evolving inclination, thus constitutes a challenging new test.

The paper is structured as follows. In § 2, model assumptions and equations are presented, simplified and cast in dimensionless form. In § 3, analytical techniques are used to derive solutions for three successive stages of avalanche evolution, characterized respectively by entrainment, bypass and detrainment. In § 4, the behaviour of the solutions is described, as a function of the dimensionless number that measures the brittleness of the slope. In § 5, comparisons are made with experiments and discrete element simulations. Section 6, finally, is devoted to conclusions and avenues for future work.

2. Model formulation

2.1. *Model equations and assumptions*

As illustrated by figure 1(*a*), we consider dry granular avalanches down erodible slopes of surface inclination θ close to the critical angle θ_c, and choose axes (x, z) tilted at this angle. We denote by $\tilde{z}(x, t)$ and $\underset{\sim}{z}(x, t)$ the upper and lower boundaries of the flow layer, with $h(x, t) = \tilde{z} - \underset{\sim}{z}$ the corresponding thickness. Local governing equations are then applied to domain $\underset{\sim}{z} < z < \tilde{z}$, subject to the following assumptions. In a drum of width W,

we consider solid grains of diameter D and density ρ_S, and assume dense granular flows for which the solid fraction c_S and bulk density $\rho = c_S\rho_S$ are approximately constant, as supported by experimental observations (MiDi 2004). Although the transition from static to flowing typically involves some degree of dilatancy, the resulting changes in volume fraction are assumed small enough to be negligible. Mass conservation therefore reduces to the continuity equation

$$\frac{\partial u}{\partial x} + \frac{\partial w}{\partial z} = 0, \tag{2.1}$$

where u, w are the downslope and normal components of velocity. Secondly, shallow flows are assumed, hence local momentum balance equations parallel and normal to the slope can be written

$$\rho\left(\frac{\partial u}{\partial t} + u\frac{\partial u}{\partial x} + w\frac{\partial u}{\partial z}\right) = \rho g\sin\theta + \frac{\partial\tau}{\partial z}, \tag{2.2}$$

$$\frac{\partial\sigma}{\partial z} = -\rho g\cos\theta, \tag{2.3}$$

where τ and σ are respectively the shear and normal granular stresses, and g is the gravitational acceleration. Transverse velocity variations are neglected, and the flows are assumed sufficiently shallow and wide to neglect the influence of sidewall friction. For some granular flows in thin channels, sidewall friction plays a crucial role, as it controls the flow depth attained at steady state over erodible beds (Taberlet *et al.* 2003; Jop *et al.* 2005). Episodic surface avalanches, however, also occur in wide drums, or in discrete element simulations for which sidewalls are replaced by periodic boundary conditions (Han *et al.* 2021). This indicates that sidewall friction is not a crucial factor for unsteady, discrete avalanching. Even when frictional sidewalls are present, in this work we will assume for simplicity that the ratio of flow depth to drum width remains small enough for sidewall friction to be negligible.

For the shear stress τ within the flow layer, we assume the linearized $\mu(I)$ rheology (da Cruz *et al.* 2005)

$$\tau = \mu(I)\sigma = (\tan\theta_c + \chi\sqrt{\rho/\rho_S}I)\sigma = \tan\theta_c\sigma + \chi D\sqrt{\rho\sigma}\dot{\gamma}, \tag{2.4}$$

where μ is the dimensionless shear to normal stress ratio, χ a dimensionless rheological coefficient, $\dot{\gamma} = \partial u/\partial z$ the local shear rate and $I = \dot{\gamma}D/\sqrt{\sigma/\rho_S}$ the inertial number. For sustained shear at very slow shear rate, $I \ll 1$, the ratio of shear to normal stress therefore reduces to $\tau/\sigma = \tan\theta_c$, which defines the critical angle of internal friction θ_c. As $\dot{\gamma}$ increases, τ increases proportionately, with an effective viscosity $\chi D\sqrt{\rho\sigma}$ that varies as the square root of the normal stress σ. For frictional spheres, experiments (Jop *et al.* 2005; Tapia *et al.* 2019) and discrete element simulations (Azéma & Radjaï 2014) show that the rheological coefficient does not vary greatly with particle properties, and takes the approximate value $\chi \approx 1$. For frictionless particles, simulations with two-dimensional (Bouzid *et al.* 2013) and three-dimensional grains (Dumont *et al.* 2023) indicate that, instead of a linear relationship, the rate-dependent component of the shear stress varies roughly with the square root of the shear rate. In this work, we restrict our attention to frictional spheres.

Boundary conditions at the surface and at the base of the flowing layer are formulated as follows. First, we assume zero flux across the free surface $z = \tilde{z}$, hence the kinematic

boundary condition

$$\frac{\partial \tilde{z}}{\partial t} + \tilde{u}\frac{\partial \tilde{z}}{\partial x} = \tilde{w}, \tag{2.5}$$

where $\tilde{u}$, $\tilde{w}$ denote the velocity components along the free surface. At the surface, we also assume no stress, or $\tilde{\tau} = \tilde{\sigma} = 0$. The normal stress then integrates to $\sigma = \rho g_\perp y$, where $g_\perp = g\cos\theta_c$ and $y = \tilde{z} - z$ denotes the depth below free surface. Assuming the rheology (2.4), the shear rate must therefore vanish at the upper free surface. This is at variance with experiments (Capart *et al.* 2015) and discrete element simulations (Parez *et al.* 2016), which show instead a finite shear rate at the top. The resulting velocity profiles, however, remain in relatively close agreement.

At the base, we adopt the new boundary conditions proposed recently by Capart (2023) for granular flows over brittle beds. Flow is assumed to take place over an erodible granular substrate, or bed, with which grains can be exchanged. The basal boundary $z = \underset{\sim}{z}$, representing the interface between the flow and bed, is defined as the uppermost locus where $\Delta u = 0$, with Δu denoting the granular velocity in excess of the bed velocity due to rigid body rotation. For slow drum rotation rates, the bed rotation velocity can be neglected, as it is much smaller than the velocity of avalanching grains. Regardless, the decrease of the excess velocity Δu to zero at a well-defined finite depth is again an idealization, as actual velocity profiles typically show a more gradual exponential decay or power law decrease to zero at the base.

Subject to this idealization, the basal interface constitutes a sharply defined moving boundary that evolves according to

$$\frac{\partial \underset{\sim}{z}}{\partial t} - \underset{\sim}{w} = -e + d. \tag{2.6}$$

On the left-hand side, $\underset{\sim}{w}$ is the velocity at which the basal substrate uplifts ($\underset{\sim}{w} > 0$) or subsides ($\underset{\sim}{w} < 0$) due to drum rotation or sandbox tilting. On the right-hand side, $e \geq 0$ is the rate of erosion or entrainment and $d \geq 0$ the rate of deposition or detrainment, both assumed positive. Whether entrainment ($e > 0$) or detrainment ($d > 0$) can occur then depends on the shear stress $\underset{\sim}{\tau}$ and shear rate $\underset{\sim}{\dot{\gamma}}$ attained at the base of the flow layer. For erosion to occur ($e > 0$), the basal shear stress must overcome the erosion resistance

$$\tau_e = \tan\theta_e \sigma, \tag{2.7}$$

where $\theta_e > \theta_c$ is an angle of friction describing the bed resistance to erosion: a greater shear stress is needed to unjam bed grains than to keep them flowing at a slow shear rate (Atman *et al.* 2014; Farain & Bonn 2023). Note that the angle θ_e, like the failure angle θ_f, does not take a unique value. Instead, it may depend on system history and exhibit random variation from one avalanche to the next. For a single avalanche, however, we will assume θ_e to be constant. Similar to our assumed gap between θ_e and θ_c, Dumont *et al.* (2020) conducted discrete element simulations of heap and inclined plane flows of frictional spheres in which they found a significant gap between erosion and sedimentation angles.

Accordingly, when $e > 0$, the shear stress at the base of the flowing layer must satisfy

$$\underset{\sim}{\tau} = \tan\theta_e \underset{\sim}{\sigma} = \tan\theta_c \underset{\sim}{\sigma} + \chi D\sqrt{\rho\underset{\sim}{\sigma}}\,\underset{\sim}{\dot{\gamma}}, \tag{2.8}$$

where $\underset{\sim}{\sigma} = \rho g_\perp h$ is the normal stress at the base. For entrainment to occur, the requisite shear stress must be provided by rapidly sheared near-bed grains. Thus the basal shear rate
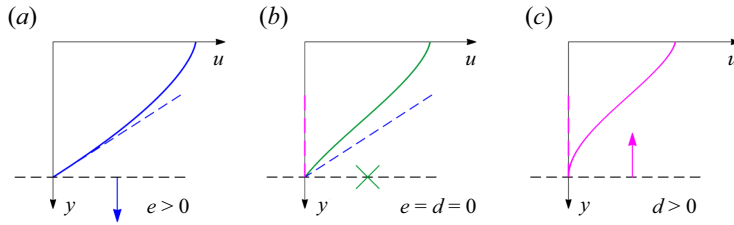
Figure 2. Three possible solution behaviours dependent on the basal shear rate: (*a*) entrainment, possible only when the shear rate is maximal (dashed blue line); (*b*) bypass, when the basal shear rate is intermediate; (*c*) detrainment, possible only when the basal shear rate is zero (dashed magenta line). Arrows up or down denote basal interface motions, and a cross the absence of such motion.

has to reach the maximal value

$$\dot{\gamma}_{max} = \frac{\tan\theta_e - \tan\theta_c}{\chi D}\sqrt{g_\perp h}, \tag{2.9}$$

proportional to the difference between the two friction coefficients $\tan\theta_e$ and $\tan\theta_c$. For detrainment to occur ($d > 0$), on the other hand, we assume that the basal shear rate must decrease to zero. The entrainment and detrainment rates e, d are therefore governed by the following complementary inequalities

$$e \geq 0, \quad \dot{\gamma} \leq \dot{\gamma}_{max}, \quad (\dot{\gamma} - \dot{\gamma}_{max})e = 0, \tag{2.10a–c}$$

$$d \geq 0, \quad \dot{\gamma} \geq 0, \quad \dot{\gamma}d = 0. \tag{2.11a–c}$$

By eroding or depositing grains as needed, the flow layer thus maintains its basal shear rate within a finite range, bracketed by the following lower and upper bounds:

$$0 \leq \dot{\gamma} \leq \dot{\gamma}_{max}. \tag{2.12}$$

Conversely, these bounds must be attained for the flow to erode or deposit grains. If the bounds are not attained, $0 < \dot{\gamma} < \dot{\gamma}_{max}$, we assume that the flow can neither entrain or detrain, and call this situation bypass. These three possible basal behaviours – entrainment, bypass and detrainment – are illustrated in figure 2. As the flow evolves over time, the conditions (2.10a–c) and (2.10a–c) allow the flow to transition continuously between these three behaviours.

2.2. *Reduced equations*

Integrated over depth, the local continuity equation (2.1) yields an evolution equation for the surface profile $\tilde{z}(x, t)$

$$\frac{\partial \tilde{z}}{\partial t} + \frac{\partial q}{\partial x} = w, \tag{2.13}$$

where $q = \int u \, dz$ is the discharge per unit width. Upon invoking (2.6), we can then deduce

$$\frac{\partial h}{\partial t} + \frac{\partial q}{\partial x} = e - d. \tag{2.14}$$

The erosion and deposition rates e, d thus affect the evolution of the flow thickness h, but do not directly affect the evolution of the free surface elevation $\tilde{z}$. For application to

988 A27-6

rotating drums, the basal velocity $\underset{\sim}{w}$ induced by drum rotation can be expressed

$$\underset{\sim}{w} = -\Omega x, \tag{2.15}$$

where Ω is the drum rotation rate, and with the origin $x = 0$ placed at mid-slope. When the drum is slowly rotated, episodic avalanches occur, during which the surface inclination drops rapidly, alternating with periods of no flow and gradual re-steepening. Both during and between slope relaxation events, experiments indicate that the surface profile $\tilde{z}(x, t)$ can be well approximated by a straight line of time-varying inclination

$$\tilde{z}(x, t) = -(\theta(t) - \theta_c)x. \tag{2.16}$$

Substitution of (2.15) and (2.16) into (2.13) produces

$$\frac{\partial q}{\partial x} = \left(\frac{\mathrm{d}\theta}{\mathrm{d}t} - \Omega\right)x. \tag{2.17}$$

Integration subject to boundary conditions $q = 0$ at $x = \pm L/2$ then yields

$$q(x, t) = \frac{(L/2)^2 - x^2}{2}\left(\Omega - \frac{\mathrm{d}\theta}{\mathrm{d}t}\right). \tag{2.18}$$

By assuming that the free surface remains perfectly straight, with a time-dependent but uniform inclination, we therefore constrain the flow discharge to evolve synchronously everywhere along the slope. Thus we neglect the local surface irregularities and propagation dynamics that can be observed in both experiments (Balmforth & McElwaine 2018) and discrete element simulations (Han *et al.* 2021). In what follows, we will assume very slow steepening rates ($\Omega \ll -\mathrm{d}\theta/\mathrm{d}t$) and focus on the comparatively fast slope relaxation events. Applying (2.18) at mid-slope then yields for the inclination $\theta(t)$ the ordinary differential equation (Courrech du Pont *et al.* 2005)

$$\frac{\mathrm{d}\theta}{\mathrm{d}t} = -\frac{8}{L^2}q(0, t), \tag{2.19}$$

involving only the discharge $q(0, t)$ at mid-slope ($x = 0$), where $\tilde{z}(0, t) = 0$. At mid-slope, moreover, $\partial q/\partial x = 0$ and the flow is approximately uniform, so that convective acceleration terms can be safely neglected. The local momentum balance equation (2.2) can therefore be approximated there by

$$\rho\frac{\partial u}{\partial t} = \rho g \sin\theta + \frac{\partial \tau}{\partial z}. \tag{2.20}$$

Substitution of the rheology (2.4) then yields

$$\frac{\partial u}{\partial t} = g_\perp(\tan\theta - \tan\theta_c) + g_\perp^{1/2}\chi D\frac{\partial}{\partial y}\left(y^{1/2}\frac{\partial u}{\partial y}\right), \tag{2.21}$$

where it is convenient to use the depth coordinate $y = \tilde{z} - z$ instead of z. Upon defining the excess slope $S(t)$ by

$$S(t) = \tan\theta(t) - \tan\theta_c, \tag{2.22}$$

we can approximate $\mathrm{d}\theta/\mathrm{d}t = \cos^2\theta_c\,\mathrm{d}S/\mathrm{d}t$. We can therefore describe the relaxation of slopes of finite length using two coupled equations. The first is an ordinary differential

equation for the excess slope

$$\cos^2 \theta_c \frac{dS}{dt} = -\frac{8}{L^2} \int_0^h u \, dy, \quad (2.23)$$

featuring on the right-hand side the integral of the velocity profile at mid-slope, $u(y, t)$. The second is a partial differential equation for this velocity profile

$$\frac{\partial u}{\partial t} = g_\perp S(t) + g_\perp^{1/2} \chi D \frac{\partial}{\partial y} \left(y^{1/2} \frac{\partial u}{\partial y} \right) \quad (0 < y < h), \quad (2.24)$$

where the excess slope $S(t)$ intervenes as a time-dependent forcing term. The velocity profile is subject to three boundary conditions, one at the free surface and two at the base

$$\frac{\partial u}{\partial y} = 0 \quad (y = 0), \quad (2.25)$$

$$u = 0, \quad 0 \le -\frac{\partial u}{\partial y} \le \frac{\tan \theta_e - \tan \theta_c}{\chi D} \sqrt{g_\perp h} \quad (y = h). \quad (2.26)$$

Two boundary conditions are needed at the base because the time-evolving flow thickness $h(t)$ is also unknown. For the initial conditions, finally, we assume that the granular slope starts from rest, at failure time t_f and failure angle θ_f, with a flow layer of zero initial thickness $h_f = 0$.

Assuming slow rotation rates, note that the equations derived here apply to arbitrary drum fill level l, the influence of which we capture via the slope length L. Following Gray (2001), we define the fill level l as the offset distance of the flat free surface away from the drum centre. The slope length is then $L = 2\sqrt{R^2 - l^2}$, and reduces to $L = 2R$ when the drum is half-filled ($l = 0$). Provided that the correct slope length L is used, all our results continue to hold when $l \ne 0$, motivating our choice of L instead of R as our defining length. In § 5, we will need this flexibility to apply the theory to the discrete element simulations of Kasper *et al.* (2021), for which the drum was not half-filled. Prior to solving the equations, it is useful to first cast them in dimensionless form. For this purpose, a scaling analysis is conducted in the next section.

2.3. *Scaling analysis*

To make the equations dimensionless, let us adopt the slope length L as length scale, and $S_e = \tan \theta_e - \tan \theta_c$ as slope scale. We then seek time, velocity and depth scales T, U and H that balance the different terms of the reduced equations. From (2.23), we deduce

$$\cos^2 \theta_c \frac{S_e}{T} = \frac{HU}{L^2}. \quad (2.27)$$

From (2.24), on the other hand, we get

$$\frac{U}{T} = g_\perp S_e = \frac{g_\perp^{1/2} \chi D U}{H^{3/2}}. \quad (2.28)$$

For the depth scale, we obtain

$$H = (\chi DL \cos \theta_c)^{1/2}. \quad (2.29)$$

The depth scale H is therefore proportional to the geometric mean of the grain diameter D and slope length L, a surprisingly simple result that does not seem to have been

reported previously. For the time scale, we deduce

$$T = \frac{(L\cos\theta_c)^{3/4}}{g_\perp^{1/2}(\chi D)^{1/4}}, \qquad (2.30)$$

proportional to the slope length L raised to the power $3/4$, and inversely proportional to the grain diameter D to the power $1/4$. For the velocity scale, finally, we get

$$U = g_\perp^{1/2}\frac{(L\cos\theta_c)^{3/4}}{(\chi D)^{1/4}}S_e, \qquad (2.31)$$

proportional to the slope scale S_e. We use these scales to define the dimensionless variables

$$y^* = \frac{y}{H}, \quad h^* = \frac{h}{H}, \quad t^* = \frac{t-t_f}{T}, \quad S^* = \frac{S}{S_e}, \quad u^* = \frac{u}{U}, \quad \dot\gamma^* = \frac{\dot\gamma}{U/H}. \quad (2.32a\text{--}f)$$

The governing equations then become, in dimensionless form,

$$\frac{\mathrm{d}S^*}{\mathrm{d}t^*} = -8\int_0^{h^*} u^*\,\mathrm{d}y^*, \qquad (2.33)$$

$$\frac{\partial u^*}{\partial t^*} = S^* + \frac{\partial}{\partial y^*}\left(y^{*1/2}\frac{\partial u^*}{\partial y^*}\right), \qquad (2.34)$$

with boundary conditions

$$\frac{\partial u^*}{\partial y^*} = 0 \quad (y^* = 0), \qquad (2.35)$$

$$u^* = 0, \quad 0 \le -\frac{\partial u^*}{\partial y^*} \le h^{*1/2} \quad (y^* = h^*), \qquad (2.36)$$

and initial conditions

$$h^* = 0, \quad S^* = S_f^* = \frac{\tan\theta_f - \tan\theta_c}{\tan\theta_e - \tan\theta_c} \approx \frac{\theta_f - \theta_c}{\theta_e - \theta_c} \quad (t^* = t_f^* = 0). \qquad (2.37)$$

The number S_f^*, the only dimensionless number that remains, represents the over-steepening of the slope at failure. It is defined as the ratio of excess slope at failure to excess resistance to erosion. Remarkably, the failure and erosion resistance inclinations θ_f and θ_e affect the dimensionless dynamics of discrete avalanches only jointly, via this number S_f^*. Analogous to the brittleness index introduced by Bishop (1971), it provides a dimensionless measure of the brittleness, or degree of metastability of the slope.

Mathematically, we obtain a rather unusual system coupling one integro-differential equation for the slope $S^*(t^*)$ (2.33), with one partial differential equation for the velocity profile $u^*(y^*, t^*)$ (2.34). To solve this system, we need to examine in sequence three distinct stages, characterized respectively by entrainment, bypass and detrainment. In the next section, analytical techniques will be used to derive solutions for each stage.

3. Solution derivation

3.1. *Entrainment stage*

Upon failure, the avalanching layer must first entrain grains from the underlying substrate. For erosion to occur, the basal shear rate must attain its upper limit

$$-\frac{\partial u^*}{\partial y^*}(y^* = h^*) = \dot{\gamma}^*_{max} = h^{*1/2}. \tag{3.1}$$

By analogy with the constant slope case treated in Capart (2023), we seek an exact similarity solution whereby the flowing layer simultaneously thickens and accelerates, while maintaining a velocity profile of Bagnold shape. The time-evolving velocity profile satisfying the boundary conditions at the surface and at the base is then

$$u^*(y^*, t^*) = \begin{cases} \frac{2}{3}(h^*(t^*)^{3/2} - y^{*3/2}), & 0 \le y^* \le h^*(t^*), \\ 0, & h^*(t^*) \le y^*, \end{cases} \tag{3.2}$$

where $h^*(t^*)$ is the flow thickness evolution, yet to be determined. Substituting this ansatz into the mass and momentum balance equations (2.33) and (2.34) yields

$$\frac{\mathrm{d}S^*}{\mathrm{d}t^*} = -\frac{16}{5}h^{*5/2}, \tag{3.3}$$

$$h^{*1/2}\frac{\mathrm{d}h^*}{\mathrm{d}t^*} = S^* - 1, \tag{3.4}$$

which form a pair of nonlinear ordinary differential equations (ODEs) for the coupled time evolution of the avalanche slope $S^*(t^*)$ and thickness $h^*(t^*)$. Note that the Bagnold velocity profile does not represent an extra assumption or approximation on our part, nor is it restricted to flows over a non-erodible base. For the entrainment stage, the time-evolving Bagnold profile (3.2) is the exact solution to the assumed governing equations, boundary and initial conditions, provided that the two ODEs (3.3) and (3.4) are satisfied. This was derived step by step in Capart (2023), and can be checked by direct substitution into (2.33) to (2.37). During bypass and detrainment, the Bagnold shape no longer applies and the velocity profile deforms into a sigmoidal shape.

To solve the equations, the time variable can be eliminated from (3.4) by using the chain rule together with (3.3), yielding the separable ODE

$$h^{*1/2}\frac{\mathrm{d}h^*}{\mathrm{d}S^*}\frac{\mathrm{d}S^*}{\mathrm{d}t^*} = -\frac{16}{5}h^{*3}\frac{\mathrm{d}h^*}{\mathrm{d}S^*} = S^* - 1. \tag{3.5}$$

This can be integrated with initial conditions $S^* = S^*_f$ and $h^* = 0$ at time $t^*_f = 0$, to get

$$h^*(S^*) = \left(\frac{5}{8}\right)^{1/4}((S^*_f - 1)^2 - (S^* - 1)^2)^{1/4}. \tag{3.6}$$

The flow layer thickness increases until $S^* = S^*_e = 1$, where it saturates at the extremal value

$$h^*_e = \left(\frac{5}{8}\right)^{1/4}(S^*_f - 1)^{1/2}, \tag{3.7}$$

retained during the ensuing bypass stage. By integrating the profile (3.2) over depth, we can also calculate the discharge evolution

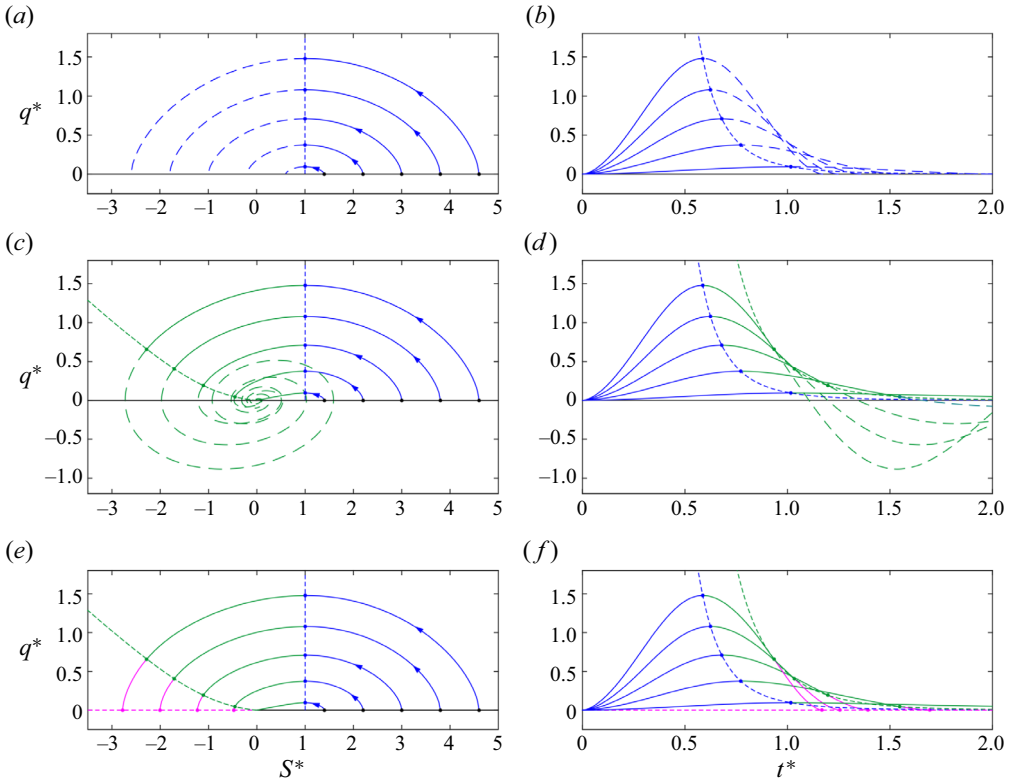$$q^*(S^*) = \frac{2}{5}\left(\frac{5}{8}\right)^{5/8}((S^*_f - 1)^2 - (S^* - 1)^2)^{5/8}. \tag{3.8}$$

Figure 3. Solution curves for slopes of varying brittleness, during successive evolution stages: (a,b) solutions for the entrainment stage (blue lines) and their continuation beyond their domain of validity (long blue dashes); (c,d) solutions for the bypass stage (green lines) and their continuation beyond their domain of validity (long green dashes); (e,f) solutions for the detrainment stage (magenta lines). Short dashes: domain boundaries.

The resulting orbits are shown in figure 3(a), for five different values of S_f^*. The discharge peaks at the end of the entrainment stage ($S^* = S_e^* = 1$), reaching the maximum value

$$q_e^* = \tfrac{2}{5} \left(\tfrac{5}{8} \right)^{5/8} (S_f^* - 1)^{5/4}. \tag{3.9}$$

Upon defining $S' = S^* - 1$, $\hat{S}' = S'/S_f'$ and $\hat{q} = q^*/q_e^*$, the slope–discharge relationship can also be written

$$\hat{S}'^2 + (\hat{q}^{4/5})^2 = 1. \tag{3.10}$$

In the $(\hat{S}', \hat{q}^{4/5})$ plane, the orbits trace a unit circle centred at the origin. In the (S^*, q^*) plane, as illustrated in figure 3(a), the orbits become slightly distorted. Different failure slopes S_f^* yield geometrically similar orbits (scaled copies of each other) with similarity centre $(S_e^*, 0) = (1, 0)$. Starting from rest, no self-accelerating erosion can occur if $S_f^* \le 1$. Beyond this threshold, the greater the oversteepening at failure, the greater the maximum discharge attained by the resulting avalanche.

To obtain the time evolution, the solution (3.6) can be substituted back into (3.3) to get

$$\frac{\mathrm{d}S^*}{\mathrm{d}t^*} = -2 \left(\frac{8}{5} \right)^{3/8} ((S_f^* - 1)^2 - (S^* - 1)^2)^{5/8}. \tag{3.11}$$

Defining $\hat{t} = 2(\frac{8}{5})^{3/8} S_f'^{1/4} t^*$, this ODE can be normalized and separated into

$$\frac{d\hat{S}'}{(1 - \hat{S}'^2)^{5/8}} = -d\hat{t}. \tag{3.12}$$

Integration subject to initial condition $\hat{S}'(0) = 1$ then yields the implicit solution

$$G_{5/4}(\hat{S}') - G_{5/4}(1) = -\hat{t}. \tag{3.13}$$

Here, we have introduced the generalized arcsine function

$$G_\varphi(x) = \int_0^x \frac{d\xi}{(1 - \xi^2)^{\varphi/2}} = x {}_2F_1\left(\frac{1}{2}, \frac{\varphi}{2}; \frac{3}{2}; x^2\right), \tag{3.14}$$

where ${}_2F_1(a, b; c, x)$ is the hypergeometric function. Defined over interval $-1 \le x \le 1$, $G_\varphi(x)$ is an odd function that resembles an arcsine and in fact reduces to $G_1(x) = \sin^{-1}(x)$ when $\varphi = 1$. The normalized time at which $\hat{S}' = 0$, erosion ends and the discharge peaks is then given by

$$\hat{t}_e = G_{5/4}(1) = \int_0^1 \frac{dx}{(1 - x^2)^{5/8}} = \frac{\sqrt{\pi}\,\Gamma\left(\frac{3}{8}\right)}{2\Gamma\left(\frac{7}{8}\right)} \approx 1.9279, \tag{3.15}$$

where $\Gamma(\cdot)$ is the gamma function. In terms of dimensionless variables (2.36), this result can also be written

$$t_e^* = \frac{1}{2}\left(\frac{5}{8}\right)^{3/8} \hat{t}_e(S_f^* - 1)^{-1/4} = \frac{1}{4}\left(\frac{5}{2}\right)^{3/10} \hat{t}_e q_e^{*-1/5}. \tag{3.16}$$

Thus the greater the oversteepening at failure, the greater the peak discharge, and the shorter the time needed to attain this peak. This is illustrated in figure 3(b), which shows the dimensionless discharge hydrographs $q^*(t^*)$ associated with the orbits of figure 3(a). Note that the results of this section are valid only for the entrainment stage, over time interval $t_f^* = 0 \le t^* \le t_e^*$. The corresponding curve segments are shown as solid lines on figure 3(a,b). To show what the formulas produce beyond this range of validity, however, the corresponding curves are also shown as dashed lines. The correct curves for $t^* > t_e^*$ are derived in the next sections.

3.2. *Bypass stage*

At time $t^* = t_e^*$, the flow layer starts to decelerate. Detrainment cannot yet occur, however, because the basal shear rate $\dot{\underset{\sim}{\gamma}}^*$ at this time still has the maximal value

$$\dot{\underset{\sim}{\gamma}}_{max}^* = h_e^{*1/2}. \tag{3.17}$$

Starting from this finite value, the basal shear rate must drop back to zero before deposition can occur. Over some time $t_e^* \le t^* \le t_d^*$, the flowing layer will therefore undergo bypass, during which it will retain the constant thickness $h^* = h_e^*$ given by (3.7). During the bypass

stage, the Bagnold shape (3.2) no longer holds, hence the evolving shape of the velocity profile must be derived anew. The equations to be solved can be written

$$\frac{dS^*}{dt^*} = -8h_e^* \int_0^1 u^* \, d\eta,\tag{3.18}$$

$$\frac{\partial u^*}{\partial t^*} = S^* + \frac{1}{h_e^{*3/2}} \frac{\partial}{\partial \eta}\left(\eta^{1/2}\frac{\partial u^*}{\partial \eta}\right),\tag{3.19}$$

where $\eta = y/h = y^*/h^*$ is a normalized depth coordinate, and where the evolving velocity profile $u^*(\eta, t^*)$ must satisfy the homogeneous boundary conditions

$$\frac{\partial u^*}{\partial \eta}(0, t^*) = 0, \quad u^*(1, t^*) = 0.\tag{3.20a,b}$$

Given at time $t^* = t_e^*$, the initial conditions for the slope and velocity profile are

$$S^*(t_e^*) = 1, \quad u^*(\eta, t_e^*) = \tfrac{2}{3}h_e^{*3/2}(1 - \eta^{3/2}),\tag{3.21a,b}$$

as obtained in the previous section. Whereas for the entrainment stage a nonlinear moving boundary problem had to be solved, here the flow thickness remains constant. The equations therefore become linear and homogeneous: they are linear in the two unknowns S^* and u^*, and admit the solution pair $u^* = 0$, $S^* = 0$. Moreover, their behaviour depends on the single dimensionless number $h_e^* = (\tfrac{5}{8})^{1/4}(S_f^* - 1)^{1/2}$, which itself depends only on the oversteepening at failure, S_f^*.

Generalizing an approach applied earlier by Parez *et al.* (2016) and Capart (2023) to the constant slope case, we seek series solutions for $S^*(t)$ and $u^*(\eta, t^*)$ of the form

$$S^*(t^*) = \sum_{n=1}^{N} C_n \exp(-\lambda_n(t^* - t_e^*)),\tag{3.22}$$

$$u^*(\eta, t^*) = \sum_{n=1}^{N} C_n f_n(\eta) \exp(-\lambda_n(t^* - t_e^*)),\tag{3.23}$$

where the roots λ_n and coefficients C_n can be real or complex, and the infinite series is truncated to a finite number of terms $N = 8$ (in practice, $N = 3$ is sufficient for accuracy to at least three significant figures). The eigenfunctions $f_n(\eta)$ that satisfy the partial differential equation (3.19) and boundary conditions (3.20a,b) are obtained as

$$f_n(\eta) = \frac{\eta^{1/4}J_{-1/3}(\kappa_n\eta^{3/4}) - J_{-1/3}(\kappa_n)}{\lambda_n J_{-1/3}(\kappa_n)},\tag{3.24}$$

where $\kappa_n = \tfrac{4}{3}\lambda_n^{1/2}h_e^{*3/4}$, and $J_\nu(z)$ is the Bessel function of the first kind of order ν. To satisfy (3.18), the roots λ_n must satisfy the transcendental equation

$$K(\lambda) = (\lambda^2 + 8h_e^*)J_{-1/3}(\kappa) - 8h_e^{*1/4}\frac{J_{2/3}(\kappa)}{\lambda^{1/2}} = 0,\tag{3.25}$$

in which $\kappa = \tfrac{4}{3}\lambda^{1/2}h_e^{*3/4}$. Note that $K(\lambda)$ is a complex-valued function of a complex variable, hence we must find roots λ in the complex plane that zero both its real and imaginary parts. The condition (3.25) yields infinitely many discrete roots

S_f^*	λ_1	λ_2	λ_3	C_1	C_2	C_3
1.4	0.9497	3.714	33.16	1.0690	−0.0689	−0.0000
2.2	1.0531 ± 2.2412i		14.50	0.5004 ∓ 0.4359i		−0.0008
3.0	0.7565 ± 2.7199i		9.82	0.5028 ∓ 0.9137i		−0.0056
3.8	0.6284 ± 3.0203i		7.57	0.5096 ∓ 1.3494i		−0.0187
4.6	0.5597 ± 3.2546i		6.21	0.5221 ∓ 1.7721i		−0.0431

Table 1. First calculated roots λ_n and coefficients C_n of the bypass series solution.

λ_n, $n = 1, \ldots, \infty$, indexed by taking the real part of λ_n in ascending order. For selected values of the slope brittleness S_f^*, the first three calculated roots λ_n, $n = 1, \ldots, 3$ are listed in table 1. The real parts of all roots are positive, yielding, as expected, solutions that decay over time. All roots starting from $n = 3$ are real and distinct. For $n > 3$, the values κ_n can be approximated by the zeros of $J_{-1/3}(\kappa)$, the roots obtained earlier for the constant slope case (Capart 2023). For the first three roots, however, the variable slope condition (3.25) must be used.

The character of the first two roots depends on the value of S_f^* relative to the value $S_{f,crit}^* \approx 1.4976$ at which critical damping occurs. For $1 < S_f^* < S_{f,crit}^*$, the first two roots are real and distinct, $0 < \lambda_1 < \lambda_2$. For $S_f^* > S_{f,crit}^*$, by contrast, the first two roots are complex conjugate, $\lambda_{1,2} = \alpha \pm i\beta$. The value $S_f^* = S_{f,crit}^*$ therefore marks a transition from overdamping to underdamping. For avalanching flows started from $S_f^* < S_{f,crit}^*$, the flowing layer decelerates asymptotically to zero. Likewise, the basal shear rate $\dot{\gamma}^*$ decreases asymptotically to zero, without ever reaching zero and triggering detrainment. For avalanching flows started from $S_f^* > S_{f,crit}^*$, on the other hand, the flowing layer decelerates more strongly, and reaches zero basal shear rate in finite time. This finite time $t^* = t_d^*$ at which detrainment starts is again dependent on h_e^*, or equivalently on S_f^*.

The coefficients C_n, finally, must be chosen to satisfy the initial conditions (3.20a,b). In table 1, we provide calculated values for the first three coefficients, for selected values of S_f^*. As needed to satisfy the initial condition $S^*(t_e^*) = 1$, it can be checked that the coefficients C_n sum to 1 in each case. Once the coefficients C_n are known, the time-evolving discharge can be obtained from

$$q^*(t^*) = h_e^* \int_0^1 u^*(\eta) \, \mathrm{d}\eta = \sum_{n=1}^{N} \frac{\lambda_n C_n}{8} \exp(-\lambda_n(t^* - t_e^*)). \tag{3.26}$$

Likewise the time-evolving basal shear rate can be calculated from

$$\dot{\gamma}^*(t^*) = \sum_{n=1}^{N} C_n' \exp(-\lambda_n(t^* - t_e^*)), \tag{3.27}$$

where

$$C_n' = -\frac{C_n}{h_e^*} \frac{\mathrm{d}f_n}{\mathrm{d}\eta}(1) = \left(\frac{J_{2/3}(\kappa_n) - J_{-4/3}(\kappa_n)}{2\lambda_n^{1/2} h_e^{*1/4} J_{-1/3}(\kappa_n)} - \frac{1}{4\lambda_n h_e^*} \right) C_n. \tag{3.28}$$

If $S_f^* > S_{f,crit}$, this basal shear rate drops to zero at the finite time t_d^*. To find this time, we approximate the series (3.27) at t_d^* by its first two terms, with complex conjugate

coefficients $C'_{1,2} = A \pm iB$, such that

$$\dot{\gamma}^*(t_d^*) \approx (2A\cos(\beta(t_d^* - t_e^*)) + 2B\sin(\beta(t_d^* - t_e^*)))\exp(-\alpha(t_d^* - t_e^*)). \qquad (3.29)$$

The time t_d^* at which $\dot{\gamma}^*(t_d^*) = 0$ is therefore obtained as

$$t_d^* \approx t_e^* + \frac{1}{\beta}\tan^{-1}(-A/B). \qquad (3.30)$$

By sampling (3.22) and (3.23) at time t_d^*, we can also determine the slope $S_d^* = S^*(t_d^*) < 0$ and velocity profile $u_d^*(\eta) = u^*(\eta, t_d^*)$ attained when detrainment starts.

   For the values of S_f^* listed in table 1, the resulting orbits $(S^*(t^*), q^*(t^*))$ are plotted in figure 3(c) (green curves). For $S_f^* = 1.4$, the solution is overdamped, and reaches the origin $(0, 0)$ without ever leaving the upper half-plane. The other orbits are underdamped, and would eventually spiral inwards to the origin if the basal shear rate did not first drop to zero. The locus $\dot{\gamma}^* = 0$ across which this occurs (short green dashes) is located in the upper left quadrant of the (S^*, q^*) plane. The flow therefore reaches zero basal shear rate before the discharge q^* becomes negative. The corresponding discharge hydrographs $q^*(t^*)$ are plotted in figure 3(d). Valid solutions for the bypass stage (continuous green lines) are restricted to the time interval $t_e^* \leq t^* \leq t_d^*$, during which the basal shear rate remains positive. The underdamped curves are also plotted beyond this range (dashed green lines), but only to show their oscillatory behaviour. The correct curves for $t^* > t_d^*$ are derived in the next section.

3.3. *Detrainment stage*

During the detrainment stage, the flow simultaneously thins and decelerates. We are thus back to a moving boundary problem, this time with a given initial velocity profile at dimensionless time $t^* = t_d^*$. For this stage an exact analytical solution is out of reach, but an approximate semi-analytical solution can be obtained. For this purpose, we let both the flow layer thickness h^* and mean velocity $\bar{u}^* = q^*/h^*$ evolve over time, but assume that the velocity profile maintains the self-similar shape

$$\frac{u^*(\eta, t^*)}{\bar{u}^*(t^*)} = \frac{u^*(\eta, t_d^*)}{\bar{u}^*(t_d^*)}, \qquad (3.31)$$

inherited from the bypass solution at time $t^* = t_d^*$. Self-similarity does not hold exactly, but is supported by numerical solutions of stopping transients (Capart *et al.* 2015; Barker & Gray 2017). Subject to this assumption, only three variables $S^*(t^*)$, $h^*(t^*)$ and $\bar{u}^*(t^*)$ suffice to describe the system. Like before, the slope must satisfy

$$\frac{\mathrm{d}S^*}{\mathrm{d}t^*} = -8h^*\bar{u}^*. \qquad (3.32)$$

Subject to the basal boundary condition $\dot{\gamma}^* = 0$, appropriate for detrainment, we integrate (2.34) over the flow depth to obtain the momentum balance equation

$$\frac{\mathrm{d}}{\mathrm{d}t^*}(h^*\bar{u}^*) = h^*S^*. \qquad (3.33)$$

Finally, we follow Capart *et al.* (2015) and integrate over depth u^* times (2.34) to obtain a balance equation for the kinetic energy of the flow layer

$$\frac{\mathrm{d}}{\mathrm{d}t^*}\left(\frac{1}{2}\varphi h^*\bar{u}^{*2}\right) = h^*\bar{u}^*S^* - \psi\frac{\bar{u}^{*2}}{h^{*1/2}}, \qquad (3.34)$$

S_f^*	t_e^*	q_e^*	t_d^*	S_d^*	q_d^*	φ	ψ	t_a^*	S_a^*
1.4	1.016	0.095	—	—	—	—	—	∞	0
2.2	0.772	0.375	1.547	-0.453	0.045	1.57	3.70	1.692	-0.474
3.0	0.680	0.709	1.197	-1.109	0.191	1.55	3.59	1.391	-1.228
3.8	0.625	1.080	1.034	-1.711	0.406	1.52	3.44	1.255	-2.000
4.6	0.587	1.479	0.935	-2.279	0.659	1.49	3.29	1.169	-2.777

Table 2. Calculated solution properties for selected values of S_f^*.

where φ (Boussinesq coefficient) and ψ are the two shape factors defined by

$$\varphi = \frac{1}{h\bar{u}^2} \int_0^h u^2 \, \mathrm{d}y, \quad \psi = \frac{h^{1/2}}{\bar{u}^2} \int_0^h y^{1/2} \dot{\gamma}^2 \, \mathrm{d}y. \tag{3.35a,b}$$

Under the similarity assumption (3.31), both φ and ψ remain constant during detrainment. Using the product rule and taking quasilinear combinations of (3.33) and (3.34), we deduce the following evolution equations for the flow depth and mean velocity:

$$\frac{1}{2}\varphi\bar{u}^* \frac{\mathrm{d}h^*}{\mathrm{d}t^*} = (\varphi - 1)h^* S^* + \psi \frac{\bar{u}^*}{h^{*1/2}}, \tag{3.36}$$

$$\frac{1}{2}\varphi h \frac{\mathrm{d}\bar{u}^*}{\mathrm{d}t^*} = (1 - \tfrac{\varphi}{2})h^* S^* - \psi \frac{\bar{u}^*}{h^{*1/2}}. \tag{3.37}$$

Together, the three equations (3.32), (3.36) and (3.37) form a closed system of three coupled nonlinear ODEs for $S^*(t^*)$, $h^*(t^*)$ and $\bar{u}^*(t^*)$. Unless $\psi = 0$ is assumed, no closed form solution could be found. The equations can, however, be integrated numerically, starting from the known initial conditions

$$S^*(t_d^*) = S_d^*, \quad h^*(t_d^*) = h_e^*, \quad \bar{u}^*(t_d^*) = \bar{u}_d^*, \tag{3.38a–c}$$

applied at the time t_d^* when bypass ends and detrainment starts. Flow stops when $\bar{u}^*$ and h^* drop to zero, at which point the arrest time t_a^* has been reached, and the slope has attained the inclination $S_a^* < 0$. Contrary to early ideas about rotating drum avalanches (Carrigy 1970), the arrest angle S_a^* is therefore not a property of the granular material, but a consequence of the avalanching process that can be predicted from the model. For selected values of S_f^*, table 2 lists the calculated values of these and other flow properties.

As plotted in figure 3(e,f) (magenta lines) the detrainment solutions provide the last missing segments of the orbits and discharge hydrographs. The complete orbits (figure 3e) adopt teardrop shapes when $S_f^* < S_{f,crit}^*$. They become ovoidal when $S_f^* > S_{f,crit}^*$ and get gradually more symmetrical as the slope brittleness S_f^* increases. The discharge hydrographs, likewise, become more symmetrical about their peaks as S_f^* increases (figure 3f). When $S_f^* > S_{f,crit}^*$, the discharge decreases to zero in finite time, and this time to arrest t_a^* occurs sooner as S_f^* increases. The behaviour of the resulting solutions is described further in the next section.

4. Solution behaviour

To further illustrate solution behaviour, time-evolving velocity profiles are shown in figure 4. Here, plots are normalized by the maximum flow thickness h_e^* and maximum
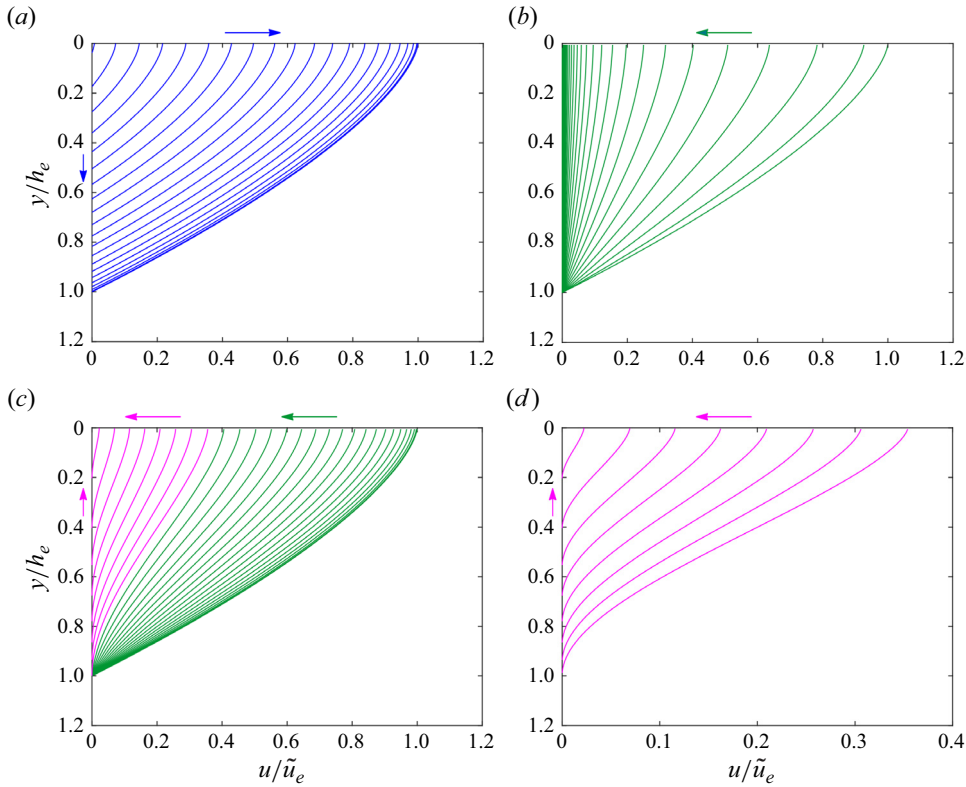
988 A27-16

Figure 4. Normalized solutions for the time-evolving velocity profile at the centreline: (*a*) entrainment stage; (*b*) bypass stage for overdamped avalanche ($S_f^* = 1.4$); (*c*) bypass (green) and detrainment (magenta) stages for underdamped avalanche ($S_f^* = 3$); (*d*) close up of detrainment stage for underdamped avalanche ($S_f^* = 3$). Arrows show direction of change: acceleration vs deceleration at the top; entrainment vs detrainment to the side. There is no detrainment stage for the overdamped case.

surface velocity $u_e^* = \frac{2}{3}(\frac{5}{8})^{3/8}(S_f^* - 1)^{3/4}$ experienced during the avalanche. During the entrainment phase (figure 4*a*), the flow simultaneously accelerates and thickens, while preserving a self-similar shape given by the Bagnold profile of (3.2). The same normalized evolution, moreover, occurs regardless of the value of the slope brittleness S_f^*. After the transition from entrainment to bypass, by contrast, the behaviour of the velocity profile becomes strongly affected by the slope brittleness. When $S_f^* < S_{f,crit}^*$ (overdamped case, figure 4*b*), the flow thickness remains constant indefinitely, and the flow layer arrests by decelerating gradually throughout its thickness. Asymptotically, the velocity profile reduces to the first term of the series (3.23), and decreases to zero over time as a negative exponential. During this deceleration, the basal shear rate always remains positive and no detrainment occurs.

When $S_f^* > S_{f,crit}^*$ (underdamped case, figure 4*c*), deceleration during the bypass stage (green lines) causes the velocity profile to gradually deform into a sigmoidal shape. As a result, the basal shear rate decreases to zero in finite time. At this point, detrainment occurs, and the ensuing velocity profiles simultaneously thin and decelerate (magenta lines, see also the close up of figure 4*d*). As the profiles shrink to zero, flow arrest occurs abruptly, also in finite time. During the deceleration phase, resistance to erosion no longer influences
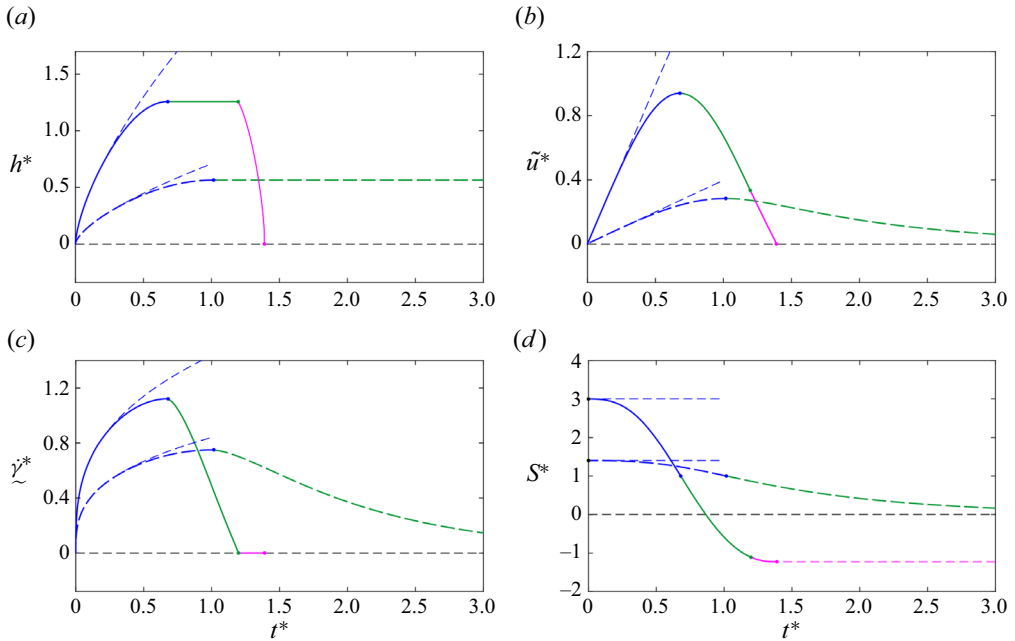
Figure 5. Time-evolving variables for overdamped ($S_f^* = 1.4$, long dashes) and underdamped avalanches ($S_f^* = 3$, continuous lines): (*a*) flowing layer thickness; (*b*) basal shear rate; (*c*) surface velocity; (*d*) surface inclination. Blue: entrainment stage (short blue dashes: response for infinitely long channel); green: bypass stage; magenta: detrainment stage. There is no detrainment stage for the overdamped case.

the evolution of the flow, and the resulting profiles agree qualitatively with numerical and analytical solutions obtained earlier for stopping flows (Barker & Gray 2017; Capart 2023).

Throughout the avalanching process, the evolving velocity profile remains continuous in both space and time. The rate of change of the velocity also remains continuous, except at the base of the flow layer upon passage of the erosion front, and at the surface upon failure and sudden arrest. To within approximation error, these continuity properties also hold across the transitions from entrainment to bypass, and from bypass to detrainment. The adopted governing equations and basal boundary conditions therefore let the flow transition freely and smoothly between entrainment, bypass and detrainment.

The time evolution of some additional solution properties is illustrated in figure 5. Figures 5(*a*) and 5(*b*) show how the flow thickness $h^*(t^*)$ and $\dot{\gamma}^*(t^*)$ jointly evolve subject to the complementary inequalities (2.10*a–c*) and (2.10*a–c*). During the entrainment stage (blue lines), both increase in algebraic lockstep, as the two quantities vary together while satisfying the quadratic relation $h^* = \dot{\gamma}_{max}^{*2}$ implied by (3.1). During the bypass stage (green lines), by contrast, the flow thickness remains constant while the basal shear rate decreases. For the overdamped case ($S_f^* = 1.4$), the basal shear rate decreases asymptotically to zero, and detrainment does not occur. For the underdamped case, the basal shear rate reaches zero in finite time, after which detrainment occurs (magenta lines) until the flow thickness has decreased to zero and flow arrest occurs.

Figure 5(*c*) shows the corresponding evolution of the surface velocity $\tilde{u}^*(t^*)$. Surface grains accelerate during the entrainment stage (blue lines), then decelerate during the bypass (green lines) and detrainment stages (magenta line). Whereas for the overdamped case, the surface velocity decreases asymptotically to zero, for the underdamped case
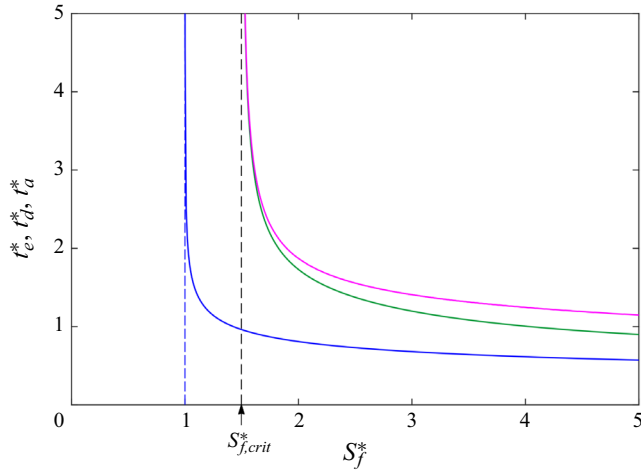
Figure 6. Dimensionless characteristic times as a function of slope brittleness. Solid lines: times at which entrainment ends (blue), detrainment starts (green) and arrest occurs (magenta). The dashed lines are the two vertical asymptotes.

the deceleration to zero occurs abruptly. Like the discharge, the surface velocity peaks at time t_e^*. The erosion resistance angle θ_e is therefore the angle at which both the discharge and surface velocity reach their maximum. This makes it straightforward to estimate from experiments or discrete element simulations. The angle of peak velocity was earlier identified by Marteau & Andrade (2018) as an important characteristic of granular avalanches.

Finally figure 5(*d*) shows the time evolution of the surface inclination during the sudden relaxation process. Immediately after failure, the inclination S^* changes slowly at first. The variables thus behave as if the channel inclination remained frozen. Accordingly, the early time evolutions of the other variables match the power laws $h^* \propto t^{*2/3}$, $\dot{\gamma}^* \propto t^{*1/3}$ and $\tilde{u}^* \propto t^*$ derived in Capart (2023) for entraining flows in channels of constant inclination (dashed blue lines in figure 5*a*–*c*). For slopes of finite length, however, the surface inclination eventually starts to drop. When the curves reach the inclination $S_e^* = 1$, they exhibit an inflection point and the flow switches from entrainment (blue lines) to bypass (green lines). In the overdamped case, the inclination then decreases asymptotically to the critical slope $S_c^* = 0$, and it takes infinite time for the flow to stop completely. Such exponentially decaying angle histories were observed by Perrin *et al.* (2019) in drum experiments involving frictionless immersed grains. In the underdamped case, by contrast, the surface inclination undershoots the critical inclination, reaching an arrest inclination S_a^* (magenta dashes) that is milder than the critical inclination $S_c^* = 0$ (black dashes), and stops evolving in finite time. Such stopping in finite time was likewise observed by Perrin *et al.* (2019) in drum experiments, when performed with frictional grains. Unlike the transition from entrainment to bypass (blue to green), the transition from bypass to detrainment (green to magenta) does not coincide with any peak or inflection point of the surface velocity or inclination history (figure 5*c*,*d*). Its occurrence hinges instead on what occurs at the base of the flow layer (figure 5*a*,*b*), more difficult to observe.

As illustrated by figure 6, the characteristic times of the avalanching process vary with the slope brittleness S_f^*. At time t_e^* (blue curve), avalanches reach their peak discharge, and transition from entrainment to bypass. This time is undefined for $S_f^* < 1$, as in that case

Test case	L (mm)	W (mm)	D (mm)	Ω (deg. s^{-1})	θ_f (deg.)	θ_c (deg.)	Θ_e (−)	$t_e - t_f$ (s)	$(d\bar{\theta}/dt)_e$ (deg. s^{-1})	Θ_a (−)	$t_a - t_f$ (s)
1	500	50	1	0.018	25.1 ± 0.3	23.7	0.45	0.83	−1.8	−0.22	1.96
2	287	110	3	0.23	27.6 ± 0.4	26.4	0.27	0.92	−1.9	−0.53	1.91
3a	118	22	2.5	3.0	29.3 ± 1.4	26.2	0.37	0.37	−8.4	−0.31	0.77

Table 3. Test conditions and model parameters determined from inclination history data. Experiments by Fischer *et al.* (2008) (case 1) and Balmforth & McElwaine (2018) (case 2); discrete particle simulations by Kasper *et al.* (2021) (case 3a).

resistance to erosion at the base prevents avalanches from growing and accelerating. For $S_f^* > 1$, t_e^* becomes shorter as the slope becomes more brittle, and diverges to infinity as $S_f^* \downarrow 1$. This limit is associated with avalanches that grow and decay infinitely slowly. At time t_d^* (green curve), avalanches transition from bypass to detrainment, and at time t_a^* they come to complete arrest (magenta curve). When $S_f^* \leq S_{f,crit}^*$, neither event occurs in finite time. For $S_f^* > S_{f,crit}^*$, by contrast, both t_d^* and t_a^* are finite, and occur sooner as the slope becomes more brittle. Both times also diverge to infinity as $S_f^* \downarrow S_{f,crit}^*$. When $1 < S_f^* \leq S_{f,crit}^*$, avalanches reach their peak discharge in finite time, but arrest infinitely slowly. Such contrasted approaches to flow arrest were observed earlier by Perrin *et al.* (2019), in drum avalanche experiments performed with frictionless and frictional immersed grains.

5. Comparison with experiments and discrete element simulations

5.1. *Data sources and processing*

To test the proposed theory, its predictions will be compared with data from three different sources: laboratory experiments by Fischer *et al.* (2008) and Balmforth & McElwaine (2018), and discrete element simulations by Kasper *et al.* (2021). The three test cases chosen, listed in table 3, are those that were described most completely in each reference. All involve frictional spherical particles in partially filled rotating drums, but the grain sizes, drum dimensions and rotation rates differ. Crucially, inclination histories featuring multiple avalanche events were reported for each test case, allowing characteristic angles to be determined. For illustration, we show in figures 7 and 8 how we processed the data from the discrete element simulations of Kasper *et al.* (2021). As explained in the original references, Fischer *et al.* (2008) and Balmforth & McElwaine (2018) used similar steps to process their own experimental data.

Illustrated in figure 7, the inclination time history $\theta(t)$ can be obtained by video analysis in experiments (Fischer *et al.* 2008; Balmforth & McElwaine 2018), or by processing particle positions in discrete element simulations (Kasper *et al.* 2021). From such time series, individual avalanche events can be identified and analysed. For each event, the (t, θ) coordinates of the maximum and minimum inclinations can first be acquired (figure 7a). These approximate the failure time and angle (t_f, θ_f), and the arrest time and angle (t_a, θ_a) associated with the event. Secondly, numerical differentiation can be used to obtain the inclination rate of change, $d\theta/dt$, and estimate from its extreme value the time, angle and angular velocity $(t_e, \theta_e, (d\theta/dt)_e)$ at the end of the entrainment phase (figure 7b).

In both simulations and experiments, avalanching is quasi-periodic (Evesque 1991), featuring a regular sequence of similar but not identical avalanches. Even after the drum has rotated at constant speed for some time, there is considerable variation
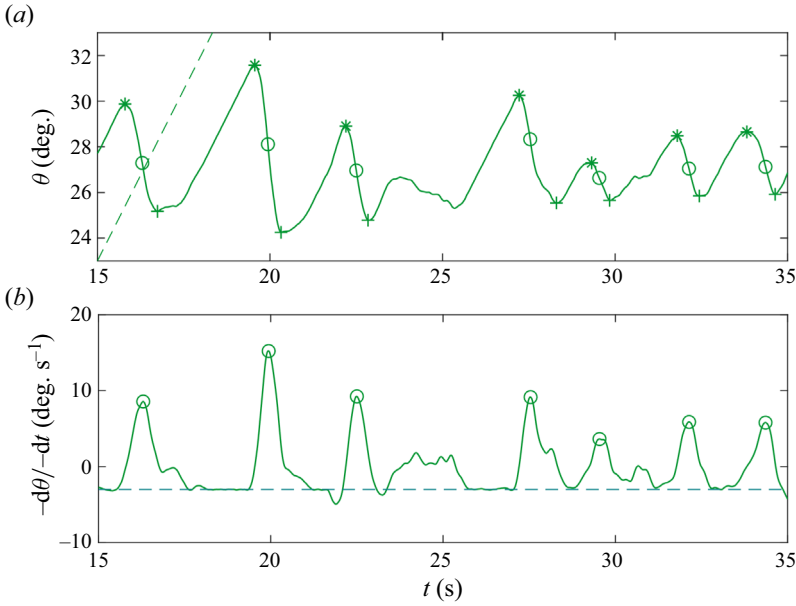
Figure 7. Processing of surface inclination history recorded in an experiment or discrete element simulation (here, a simulation by Kasper *et al.* 2021): (*a*) segmentation of angle history into separate avalanche events; (*b*) identification of extremal slope relaxation rates from numerically differentiated signal. Symbols: failure (stars), arrest (plus) and extremal values (circles). Dashes: drum rotation rate.

between successive avalanche events. In particular, a broad distribution is obtained for the avalanche amplitude $\Delta\theta = \theta_f - \theta_a$. By contrast, the avalanche and entrainment durations, $t_a - t_f$ and $t_e - t_f$, show less variation. Angle histories $\theta(t)$ for distinct avalanches, moreover, exhibit similar shapes. They were found by Balmforth & McElwaine (2018) to collapse reasonably close together when normalized in the form

$$\Phi(t) = \frac{\theta(t - t_m) - \theta_a}{\theta_f - \theta_a}, \tag{5.1}$$

where t_m is the time at which the angle crosses the midpoint value $\theta_m = (\theta_f + \theta_a)/2$. This normalized signal can therefore be averaged over multiple events to obtain the mean signal, or master curve,

$$\bar{\theta}(t) = \bar{\theta}_a + \bar{\Phi}(t)(\bar{\theta}_f - \bar{\theta}_a), \tag{5.2}$$

where $\bar{\theta}_f$ and $\bar{\theta}_a$ are mean failure and arrest angles, averaged over many avalanches. The resulting master curves are shown in figure 8(*a*,*b*), respectively, for the experiments of Balmforth & McElwaine (2018) (magenta line) and the discrete element simulations of Kasper *et al.* (2021) (green line). The master curve derived by Fischer *et al.* (2008) from 340 avalanches is also plotted on figure 8(*a*) (blue line). Note, however, that these authors used a slightly different averaging procedure, in which they also normalized the time scale (for details, see Fischer *et al.* 2008).

In their experiments (figure 8(*c*), blue dots), Fischer *et al.* (2008) found a weak, but unambiguous negative correlation between the arrest angle θ_a and the failure angle θ_f. Avalanche events that start from a higher than average failure inclination θ_f tend to stop at a lower than average arrest inclination θ_a. To describe this relationship, Fischer *et al.* (2008)
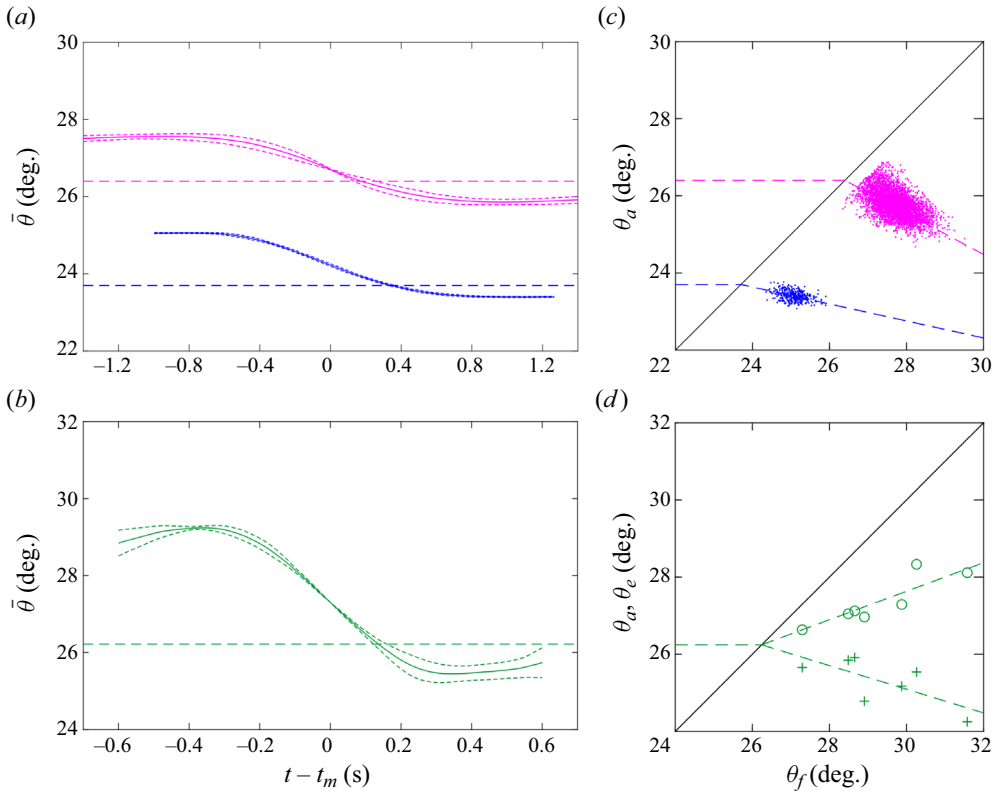
Figure 8. Master curves (*a,b*) and angle correlations (*c,d*) deduced from experiments (*a,c*) and discrete element simulations (*b,d*). Experiments by Fischer *et al.* (2008) (blue) and Balmforth & McElwaine (2018) (magenta); discrete element simulations by Kasper *et al.* (2021). Continuous lines: master curves; short dashes: ± one standard deviation; symbols: angle data from individual avalanche events; long dashes: fits through these data.

proposed a linear fit of the form

$$\theta_a = \theta_n + \Theta_a(\theta_f - \theta_n), \tag{5.3}$$

where $\Theta_a < 0$ is the slope of the best fit line, and θ_n the neutral angle defined by

$$\theta_n = \bar{\theta}_a - \frac{\Theta_a}{1 - \Theta_a}(\bar{\theta}_f - \bar{\theta}_a). \tag{5.4}$$

As illustrated by figure 8(*c*) (magenta dots), Balmforth & McElwaine (2018) found a similar negative correlation between the arrest and failure angles, for episodic avalanches produced at low drum rotation rates. At higher rotation rates, they investigated also the continuous granular flow regime. When extrapolated to zero rotation rate ($\Omega = 0$), the inclinations of their continuous flows yield inclination angles θ_1 that approximately match the neutral angles obtained from their episodic avalanches. For glass spheres of diameter 3 mm, for instance, they obtained $\theta_1 = 26.5°$, vs $\theta_n = 26.4°$ calculated from (5.4). The critical angle θ_c, defined as the friction angle under slow, sustained shear, can therefore be identified with either θ_1 or θ_n. Since θ_n can be estimated from the data for all three test cases, in this work we will set $\theta_c = \theta_n$ as calculated from (5.4).

Whereas hundreds of avalanche events were recorded in the experiments by Fischer *et al.* (2008) and Balmforth & McElwaine (2018), the simulated signal reported by

Kasper *et al.* (2021) includes only seven avalanches. Nevertheless, the data from these seven events again show a clear negative correlation (figure 8(*d*), green plus symbols). They also exhibit a clear positive correlation between θ_e and θ_f (green circles), well described by the linear fit

$$\theta_e = \theta_c + \Theta_e(\theta_f - \theta_c), \tag{5.5}$$

where $0 < \Theta_e < 1$ is the slope of the best fit line, and θ_c is again calculated using (5.4). Unfortunately, neither Fischer *et al.* (2008) nor Balmforth & McElwaine (2018) reported values of θ_e for individual avalanches. The time $t_e - t_f$, mean inclination $\bar{\theta}_e$ and angular velocity $(d\bar{\theta}/dt)_e$ at the end of the entrainment phase can nevertheless be deduced from their master curves. We can then estimate the implied correlation from

$$\Theta_e = \frac{\bar{\theta}_e - \theta_c}{\bar{\theta}_f - \theta_c}. \tag{5.6}$$

The resulting numbers are listed in table 3, together with those calculated from the discrete element simulations.

The above observations provide useful guidance for model parameterization. They imply that neither the failure angle θ_f nor the erosion angle θ_e can be taken as constant, even for avalanches taking place in identical conditions. The critical angle θ_c and the slope brittleness $S_f^* = 1/\Theta_e$, by contrast, do appear approximately constant over repeat events. Thus although θ_f and θ_e both vary from one event to another, they do so together according to the approximate relationship (5.5). This suggests that they are set by a common jamming process, undergone by the slope material prior to failure. For avalanches involving the same materials in identical conditions, we will therefore assume a constant value $S_f^* = 1/\Theta_e$, estimated from the empirical correlation Θ_e. We will also adopt the constant approximate value $\chi \approx 1$ for the rheological coefficient, except when flow thickness data are available to make a more precise determination.

To summarize, table 3 lists the two condition-dependent parameters that must be provided as inputs to the theory. They are: the critical angle, θ_c, and the erosion correlation, Θ_e. From these parameters, the complete evolution of an avalanche event can be predicted from its initial failure inclination θ_f. Table 3 also lists some additional measurements, likewise determined from the slope data, but which are not needed as model inputs. They are: the entrainment phase duration, $t_e - t_f$, the extremal rate of change of the mean inclination, $(d\bar{\theta}/dt)_e$, the arrest correlation, Θ_a, and the avalanche duration $t_a - t_f$. Among these parameters, the arrest correlation Θ_a is deduced from linear fits through the arrest inclination data (figure 8*c*,*d*). The other parameters are averaged from multiple events, when possible, or obtained from the master curve $\bar{\theta}(t)$ otherwise.

5.2. *Comparison and discussion*

As illustrated in figure 9, the parameters listed in table 3 allow various predictions of the theory to be tested. For the inclination rate of change, (3.13) governing the slope evolution during entrainment implies the dimensionless relationship

$$\frac{(d\bar{\theta}/dt)_e(t_e - t_f)}{\bar{\theta}_f - \bar{\theta}_c} = -\hat{t}_e(S_f^* - 1), \tag{5.7}$$
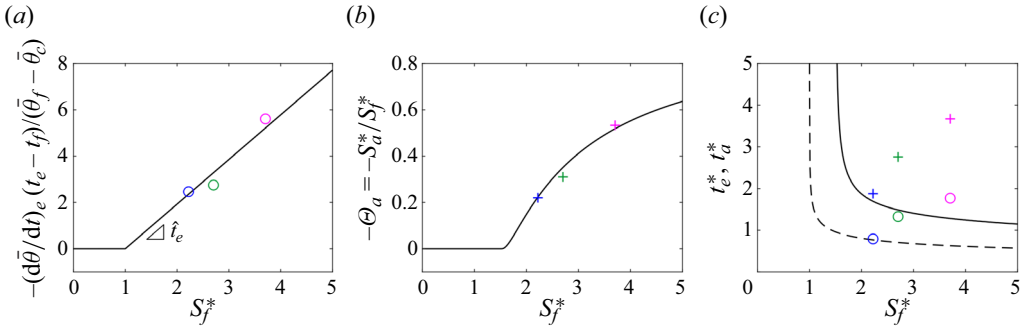
Figure 9. Comparison of predicted relationships with the data of Fischer *et al.* (2008) (blue), Balmforth & McElwaine (2018) (magenta) and Kasper *et al.* (2021) (green), for different variables as a function of slope brittleness: (*a*) extremal slope relaxation rate; (*b*) arrest inclination; (*c*) times at which entrainment ends (dashed line, circles) and arrest occurs (solid line, plus symbols).

where $\hat{t}_e$ is the numerical constant given by (3.15). The arrest correlation Θ_a, on the other hand, should satisfy the dimensionless relationship

$$\Theta_a = \frac{S_a^*(S_f^*)}{S_f^*}, \tag{5.8}$$

where $S_a^*(S_f^*)$ is the predicted under-steepening at arrest, calculated from the theory as a function of the over-steepening at failure, S_f^*. In figure 9(*a*,*b*), the two theoretical relations (5.7) and (5.8) are compared with the data for the three test cases. Excellent agreement is observed, indicating that the theory accurately describes these two characteristics of slope relaxation, associated, respectively, with entrainment and arrest.

For the avalanche and entrainment durations, the theory predicts the results

$$\frac{t_e - t_f}{T} = t_e^*(S_f^*), \quad \frac{t_a - t_f}{T} = t_a^*(S_f^*), \tag{5.9a,b}$$

where $T = (L\cos\theta_c)^{3/4}/(g_\perp^{1/2}(\chi D)^{1/4})$ is the time scale given by (2.30), and where t_e^*, t_a^* are the dimensionless times plotted earlier in figure 4. In figure 9(*c*), these model estimates are compared with the data. Agreement is good with the experimental data of Fischer *et al.* (2008), but quite poor for the other two cases. The predicted evolution is three times faster than that measured by Balmforth & McElwaine (2018), and twice faster than that simulated by Kasper *et al.* (2021). To reproduce the observed durations for these cases, we would need to adopt values of the rheological coefficient χ much smaller than the expected approximate value $\chi \approx 1$.

For the experiments of Fischer *et al.* (2008), the drum rotation rate Ω is only approximately 1 % of the peak slope relaxation rate $-(d\bar{\theta}/dt)_e$. For the test cases of Balmforth & McElwaine (2018) and Kasper *et al.* (2021), by contrast, the corresponding ratios are, respectively, 12 % and 36 % (see table 3). For these two test cases, one may therefore suspect that the discrepancy is due to the relatively faster rotation rates, compromising the approximation $\Omega \ll -d\theta/dt$ adopted to derive solutions and process the data. Because they reported more complete results for this run, the test case we selected for comparison (test case 2) corresponds to the moderate drum rotation rate $\Omega = 0.23 \deg.s^{-1}$. In their figure 14(*d*), however, Balmforth and McElwaine also reported avalanche duration data obtained in otherwise identical conditions, but for much slower

988 A27-24

rotation rates, down to $\Omega = 0.005 \deg. \, \mathrm{s}^{-1}$. This does not reduce the discrepancy, ruling out the finite rotating rate as the most likely reason.

The following other factors, not taken into account by our model, may account for the discrepancy. First, failure may not occur synchronously along the slope face, but instead nucleate locally and take time to propagate elsewhere (Balmforth & McElwaine 2018; Han *et al.* 2021). Secondly, sidewall friction or finite size effects may slow the avalanching process. As reported by Balmforth and McElwaine (see their figure 13), avalanche duration increases when the drum width W is reduced. Finally, the assumed transition between zero and finite shear rate subject to the rheology (2.4) may fail to capture important aspects of granular system evolution during the cyclic process. Some creep, for instance, may take place before yield occurs (Komatsu *et al.* 2001; Farain & Bonn 2023).

In figure 10(*a–c*), model results for the time evolution of the avalanches are compared with the master curves. To correct for the time scale discrepancy noted in the previous paragraph, for these comparisons we normalize the time coordinate by the duration of the entrainment phase, $t_e - t_f$, as was done for figure 9(*a*). When time is normalized in this way, good agreement is obtained between the predicted solutions and the recorded master curves, both for the inclination $\theta(t)$ (figure 10*a*) and for its rate of change $d\theta/dt$ (figure 10*b*), a proxy for flow rate $q(t)$, as functions of the normalized time. The shapes of the orbits (figure 10*c*) are also well reproduced. For low slope brittleness (experiments of Fischer *et al.* (2008), in blue), the flow rate curve is less sharply peaked and the orbit is more ovoidal, indicating a greater asymmetry between acceleration and deceleration. For high slope brittleness (experiments of Balmforth & McElwaine (2018), in magenta), by contrast, the flow rate curve is more sharply peaked, and the orbit more elliptical, indicating greater symmetry between acceleration and deceleration. The simulations of Kasper *et al.* (2021) (in green) are intermediate between the two experimental cases. Agreement is closest with the experiments of Fischer *et al.* (2008), which also best satisfy the assumptions of the model.

To check that the model can reproduce not just the composite master curve, but also individual avalanches, figure 10(*d–f*) compares solution curves with the two measured avalanche events reported by Fischer *et al.* (2008). For these comparisons, no adjustment or normalization is performed, and all parameters are kept the same as before save for the failure angles $\theta_f = 25.64$ and $\theta_f = 24.70$ deg. that were measured for these two events. The resulting solution curves (solid lines) are in fair agreement with the measurements (dots), supporting the ability of the model to describe individual avalanches despite their variability from one event to the next. Closer agreement (not shown), would be achieved by adjusting the critical angle θ_c and slope brittleness value S_f^* for each event, but this would undermine the predictive character of the model. Instead, the fair agreement obtained while keeping these two parameters constant suggests that they represent (approximately) intrinsic properties of the granular slope, unlike the highly variable failure and arrest angles.

Finally, the predicted velocity profiles at peak flow rate can be compared with the profiles obtained by Kasper *et al.* (2021) from discrete particle simulations. The simulations were performed with particles of three different diameters, in otherwise identical conditions. This makes it possible to test the scaling (2.29) for the dependence of the flow thickness on particle diameter and slope length. To compare theory and simulations, model parameters were set as follows. Because characteristic angles vary with grain size, and from one event to another, they were determined separately for each case (table 4). The critical angles θ_c were obtained from the angle histories reported by Kasper *et al.* (2021), using the fitting procedure of figure 8(*d*). The failure angles θ_f, on the other
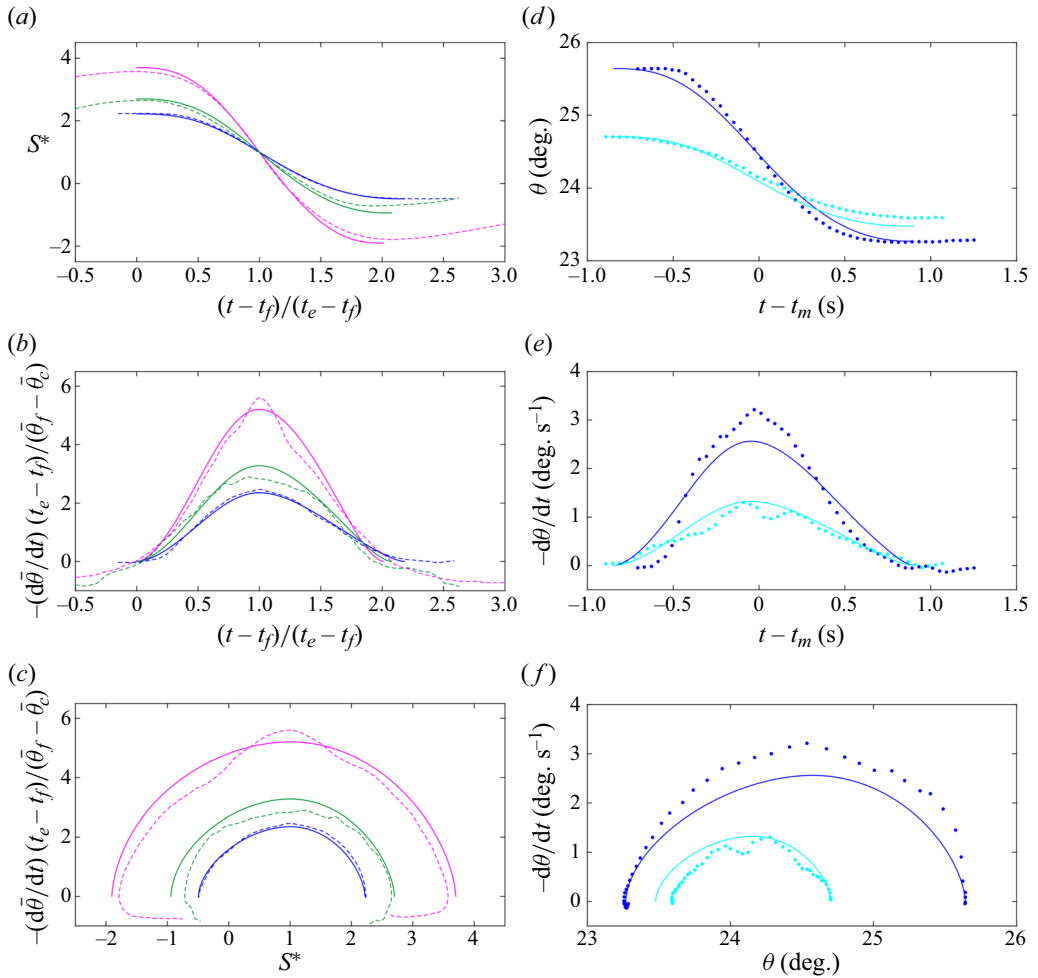
Figure 10. Comparison of predicted evolution curves with the data from Fischer *et al.* (2008) (blue, cyan), Balmforth & McElwaine (2018) (magenta) and Kasper *et al.* (2021) (green): (*a–c*) dimensionless solutions (solid lines) compared with master curve data (short dashes); (*d–f*) dimensional solutions (solid lines) compared with the data (dots) from two individual avalanche events reported by Fischer *et al.* (2008).

hand, were set by matching the peak flow rates q_e of the theory, as calculated using (3.9), with the simulated flow rates obtained by integrating the reported velocity profiles. The θ_f values deduced in this way (table 4) are somewhat higher than expected from the reported angle histories $\theta(t)$. Likewise, the integrated values q_e are higher than expected from the $(\mathrm{d}\theta/\mathrm{d}t)_e$ values of the simulated inclination histories. For the other model parameters, identical values were adopted for all three cases. For the slope brittleness, the value $S_f^* = 1/\Theta_e = 2.70$ was retained, as determined earlier from the inclination history data of figure 8(*d*). For the rheological coefficient, finally, the common value $\chi = 0.95$ was adopted, adjusted slightly from the reference value $\chi = 1$ used earlier.

The resulting comparisons are shown in figure 11(*a*). Good agreement is obtained for the velocity profile shape. Over most of the flowing layer, the simulated velocities match well the predicted Bagnold profile. At the base, however, the simulated profiles decrease to zero more gradually. Instead of the sharp drop in shear rate assumed by the model, the

Test case	L (mm)	W (mm)	D (mm)	Ω (deg. s^{-1})	θ_c (deg.)	q_e (mm^2 s^{-1})	θ_f (deg.)
3a	118	22	2.5	3.0	26.2	1525	33.9
3b	118	22	4	3.0	27.9	2670	39.3
3c	118	22	6	3.0	29.9	4280	45.2

Table 4. Test conditions and avalanche event parameters for the velocity profiles obtained by Kasper *et al.* (2021) from discrete particle simulations.
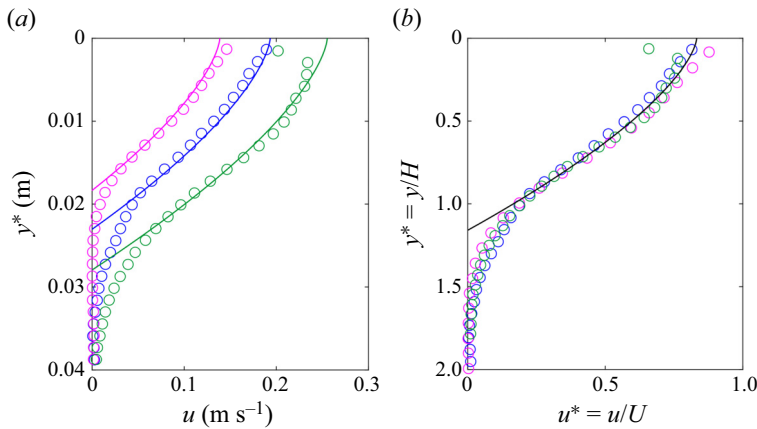

Figure 11. Comparison of predicted velocity profiles at peak flow rate (lines) with the discrete element simulations (circles) of Kasper *et al.* (2021) for three different grain diameters (magenta, $D = 2.5$ mm; blue, $D = 4$ mm; green, $D = 6$ mm) in otherwise identical conditions: (*a*) dimensional comparison; (*b*) dimensionless comparison.

simulations indicate a more gradual decrease. In earlier experiments, Courrech du Pont *et al.* (2005) measured velocity profiles along the sidewall during a single avalanche event, and found an even more diffuse, approximately exponential decrease. For steady flows over erodible heaps, models based on non-local rheology have been successful at describing velocity profiles that decay into the bed, in agreement with experiments (Komatsu *et al.* 2001). The applicability of such models to unsteady and eroding flows, however, remains uncertain (Liu & Henann 2017). In this work, we did not explore this avenue and restricted our attention to the $\mu(I)$ rheology, known to make the velocity decrease to zero at finite depth (Jop *et al.* 2005).

For the velocity magnitude, the agreement obtained is not meaningful, since we matched peak flow rates between theory and simulations. For the thickness of the flowing layer, likewise, we improved agreement by adjusting the value of the rheological coefficient. A common value for this coefficient, however, yields excellent agreement for all three grain sizes. The simulations therefore verify the predicted scaling law (2.29), whereby the characteristic thickness H of the flowing layer increases in proportion to the geometric mean of the grain diameter D and slope length L. This is further emphasized by the normalized profiles of figure 11(*b*). When plotted in dimensionless form, the simulated velocity profiles collapse closely together, and onto a common profile that matches well the predicted Bagnold shape.

6. Conclusions

In this paper, a simple continuum model of discrete granular avalanches was formulated and solved, then compared with experiments and discrete element simulations. The model assumes a linearized $\mu(I)$ rheology, and a basal erosion resistance $\tau_e = \tan\theta_e\sigma$ in excess of the critical stress $\tau_c = \tan\theta_c\sigma$ needed to sustain shear deformation. Subject to these assumptions, the model can evolve the surface inclination and mid-slope velocity profile of transient avalanches, starting from rest at the failure inclination θ_f. The resulting avalanche dynamics is controlled by well-defined thickness, velocity and time scales, together with a single dimensionless number $S_f^* = (\tan\theta_f - \tan\theta_c)/(\tan\theta_e - \tan\theta_c)$ that measures the brittleness of the slope. From inclination histories recording multiple discrete avalanches, both the critical angle θ_c and the slope brittleness S_f^* can be determined. Avalanche characteristics that can then be predicted include the peak flow rate and surface velocity, occurring when the inclination θ_e is crossed, and the arrest inclination $\theta_a \leq \theta_c$ attained when the flow ends.

The resulting solution curves and properties are in partial agreement with rotating drum experiments and discrete element simulations. Agreement is good for the arrest angle, the normalized time evolution of the slope inclination, the shape of the velocity profile at peak flow and the predicted scaling for the flow thickness, proportional to the geometric mean of the grain diameter and slope length. For the avalanche duration, however, agreement is good for one test case, but poor for the other two. To probe the remaining discrepancies, new careful experiments or discrete element simulations performed at slow drum rotation rates over multiple avalanche events would be very valuable. Detailed particle simulations could also help elucidate the grain-scale mechanisms governing slope failure and basal erosion (Atman *et al.* 2014). Likewise, the effects of finite grain size relative to channel width, slope length and flow thickness remain to be clarified.

Multiple model limitations would also need be addressed. First, the influence of interparticle friction and finite rates of drum rotation should be considered. This is necessary to model their influence on the dynamics of discrete avalanches (Allen 1970; Balmforth & McElwaine 2018), and the transition between discrete and continuous avalanching (Rajchenbach 1990; Linz *et al.* 1999; Fischer *et al.* 2009; Balmforth & McElwaine 2018; Perrin *et al.* 2019). Secondly, partial derivatives in the longitudinal and transverse directions must be included to model spatially varying flows, such as avalanches initiated from irregular terrain topography (Tai & Kuo 2008). Finally the presence of an interstitial fluid should be considered, to model liquid-immersed (Courrech du Pont *et al.* 2003), fluidized (Jessop *et al.* 2017) or liquid-driven (Gonzalez-Ondina, Liu & Fraccarollo 2022) granular flows. Such model extensions will likely require suitable numerical methods, to solve either the complete equations (see e.g. Lin & Yang 2020; Sarno *et al.* 2022) or the simpler equations obtained by integration over depth (see e.g. Capart *et al.* 2015; Edwards *et al.* 2019). Solutions obtained by analytical techniques, such as those derived in the present paper, should nevertheless remain useful to guide and verify numerical methods. These various tasks are recommended as avenues for future work.

A continuum model of discrete granular avalanches

Author ORCIDs.

Hervé Capart https://orcid.org/0000-0001-7066-3641.

REFERENCES

AGUIRRE, M.A., NERONE, N., CALVO, A., IPPOLITO, I. & BIDEAU, D. 2000 Influence of the number of layers on the equilibrium of a granular packing. *Phys. Rev.* E **62**, 738–743.

ALLEN, J.R.L. 1970 Avalanching of granular solids on dune and similar slopes. *J. Geol.* **78**, 326–351.

ALONSO-LLANES, L., MARTÍNEZ, E., BATISTA-LEYVA, A.J., TOUSSAINT, R. & ALTSHULER, E. 2022 Continuous to intermittent flows in growing granular heaps. *Phys. Rev.* E **106**, 014904.

ALTSHULER, E., TOUSSAINT, R., MARTÍNEZ, E., SOTOLONGO-COSTA, O., SCHMITTBUHL, J. & MALØY, K.J. 2008 Revolving rivers in sandpiles: from continuous to intermittent flows. *Phys. Rev.* E **77**, 031305.

ARRAN, M.I. & VRIEND, N.M. 2018 Intermittency between avalanche regimes on grain piles. *Phys. Rev.* E **97**, 060901(R).

ATMAN, A.P.F., CLAUDIN, P., COMBE, G. & MARTINS, G.H.B. 2014 Mechanical properties of inclined frictional granular layers. *Granul. Matt.* **16**, 193–201.

AZÉMA, E. & RADJAÏ, F. 2014 Internal structure of inertial granular flows. *Phys. Rev. Lett.* **112**, 078001.

BALMFORTH, N.J. & MCELWAINE, J.N. 2018 From episodic avalanching to continuous flow in a granular drum. *Granul. Matt.* **20**, 52.

BARKER, T. & GRAY, J.M.N.T. 2017 Partial regularisation of the incompressible $\mu(I)$-rheology for granular flow. *J. Fluid Mech.* **828**, 5–32.

BERZI, D., JENKINS, J.T. & RICHARD, P. 2020 Extended kinetic theory for granular flow over and within an inclined erodible bed. *J. Fluid Mech.* **885**, A27.

BISHOP, A.W. 1971 The influence of progressive failure on the choice of the method of stability analysis. *Géotechnique* **21**, 168–172.

BOUCHAUD, J.-P., CATES, M.E., RAVI PRAKASH, J. & EDWARDS, S.F. 1994 A model for the dynamics of sandpile surfaces. *J. Phys.* I **4**, 1383–1410.

BOUZID, M., TRULSSON, M., CLAUDIN, P., CLÉMENT, E. & ANDREOTTI, B. 2013 Nonlocal rheology of granular flows across yield conditions. *Phys. Rev. Lett.* **111**, 238301.

CAPART, H. 2023 Basal boundary conditions for granular surface flows over fragile and brittle erodible beds. *J. Fluid Mech.* **957**, A26.

CAPART, H., HUNG, C.-Y. & STARK, C.P. 2015 Depth-integrated equations for entraining granular flows in narrow channels. *J. Fluid Mech.* **765**, R4.

CARRIGY, M.A. 1970 Experiments on the angles of repose of granular materials. *Sedimentology* **14**, 147–158.

CHURCH, M., STOCK, R.F. & RYDER, J.M. 1979 Contemporary sedimentary environments on Baffin Island, N.W.T., Canada: debris slope accumulations. *Arctic Alpine Res.* **11**, 371–402.

COURRECH DU PONT, S., FISCHER, R., GONDRET, P., PERRIN, B. & RABAUD, M. 2005 Instantaneous velocity profiles during granular avalanches. *Phys. Rev. Lett.* **94**, 048003.

COURRECH DU PONT, S., GONDRET, P., PERRIN, B. & RABAUD, M. 2003 Granular avalanches in fluids. *Phys. Rev. Lett.* **90**, 044301.

DA CRUZ, F., EMAM, S., PROCHNOW, M., ROUX, J.N. & CHEVOIR, F. 2005 Rheophysics of dense granular materials: discrete simulation of plane shear flows. *Phys. Rev.* E **72**, 021309.

DAI, B.-B., WU, F.-Y., ZHONG, W.-T., SHI, Y.-H., QIN, J.-T., YANG, J.-J. & YANG, J. 2022 Particle sorting in scree slopes: characterization and interpretation from the micromechanical perspective. *J. Geophys. Res.* **127**, e2021JF006372.

DUMONT, D., BONNEAU, H., SALEZ, T., RAPHAËL, E. & DAMMAN, P. 2023 Microscopic foundation of the $\mu(I)$ rheology for dense granular flows on inclined planes. *Phys. Rev. Res.* **5**, 013089.

DUMONT, D., SOULARD, P., SALEZ, T., RAPHAËL, E. & DAMMAN, P. 2020 Microscopic picture of erosion and sedimentation processes in dense granular flows. *Phys. Rev. Lett.* **125**, 208002.

EDWARDS, A.N., RUSSELL, A.S., JOHNSON, C.G. & GRAY, J.M.N.T. 2019 Frictional hysteresis and particle deposition in granular free-surface flows. *J. Fluid Mech.* **875**, 1058–1095.

EVESQUE, P. 1991 Analysis of the statistics of sandpile avalanches using soil-mechanics results and concepts. *Phys. Rev.* A **43**, 2720–2740.

EVESQUE, P., FARGEIX, D., HABIB, P., LUONG, M.P. & PORION, P. 1993 Pile density is a control parameter of sand avalanches. *Phys. Rev.* E **47**, 2326–2332.

FARAIN, K. & BONN, D. 2023 Quantitative understanding of the onset of dense granular flows. *Phys. Rev. Lett.* **130**, 108201.

FISCHER, R., GONDRET, P., PERRIN, B. & RABAUD, M. 2008 Dynamics of dry granular avalanches. *Phys. Rev.* E **78**, 021302.

FISCHER, R., GONDRET, P. & RABAUD, M. 2009 Transition by intermittency in granular matter: from discontinuous avalanches to continuous flow. *Phys. Rev. Lett.* **103**, 128002.

GONZALEZ-ONDINA, J.M., LIU, P.L.-F. & FRACCAROLLO, L. 2022 Entrainment and adaptation processes in the evolution of collisional bedload layers. *Eur. J. Mech.* B*/Fluids* **92**, 132–142.

GRAY, J.M.N.T. 2001 Granular flow in partially filled slowly rotating drums. *J. Fluid Mech.* **441**, 1–29.

HAN, R., FENG, J., ZHANG, Y., YANG, H., ZIVKOVIC, V. & LI, R. 2021 Numerical simulation of avalanche propagation dynamics in a rotating drum. *Powder Technol.* **380**, 199–204.

HUNG, C.-Y., AUSSILLOUS, P. & CAPART, H. 2018 Granular surface avalanching induced by drainage from a narrow silo. *J. Fluid Mech.* **856**, 444–469.

HUNG, C.-Y., CHEN, T.-Y.K., WANG, I.-H. & HILL, K.M. 2023 Granular flows in drums of non-uniform widths. *J. Fluid Mech.* **954**, A18.

HUNG, C.-Y., STARK, C.P. & CAPART, H. 2016 Granular flow regimes in rotating drums from depth-integrated theory. *Phys. Rev.* E **93**, 030902(R).

HUNGR, O. 1995 A model for the runout analysis of rapid flow slides, debris flows, and avalanches. *Can. Geotech. J.* **32**, 610–623.

JAEGER, H.M., LIU, C. -H. & NAGEL, S.R. 1989 Relaxation at the angle of repose. *Phys. Rev. Lett.* **62**, 40–43.

JESSOP, D.E., HOGG, A.J., GILBERTSON, M.A. & SCHOOF, C. 2017 Steady and unsteady fluidised granular flows down slopes. *J. Fluid Mech.* **827**, 67–120.

JOP, P., FORTERRE, Y. & POULIQUEN, O. 2005 Crucial role of sidewalls in granular surface flows: consequences for the rheology. *J. Fluid Mech.* **541**, 167–192.

JOP, P., FORTERRE, Y. & POULIQUEN, O. 2006 A constitutive law for dense granular flows. *Nature* **441**, 727–730.

JOP, P., FORTERRE, Y. & POULIQUEN, O. 2007 Initiation of granular surface flows in a narrow channel. *Phys. Fluids* **19**, 088102.

KASPER, J.H., MAGNANIMO, V., DE JONG, S.D.M., BEEK, A. & JARRAY, A. 2021 Effect of viscosity on the avalanche dynamics and flow transition of wet granular matter. *Particuology* **59**, 64–75.

KOMATSU, T.S., INAGAKI, S., NAKAGAWA, N. & NASUNO, S. 2001 Creep motion in a granular pile exhibiting steady surface flow. *Phys. Rev. Lett.* **86**, 1757–1760.

LARCHER, M., PRATI, A. & FRACCAROLLO, L. 2018 Particle entrainment in unsteady-uniform granular avalanches. *Phys. Rev. Fluids* **3**, 124302.

LEMIEUX, P.A. & DURIAN, D.J. 2000 From avalanches to fluid flow: a continuous picture of grain dynamics down a heap. *Phys. Rev. Lett.* **85**, 4273–4276.

LI, L. & ANDRADE, J.E. 2020 Identifying spatial transitions in heterogenous granular flow. *Granul. Matt.* **22**, 52.

LIN, C.-C. & YANG, F.-L. 2020 Continuum simulation for regularized non-local $\mu(I)$ model of dense granular flows. *J. Comput. Phys.* **420**, 109708.

LINZ, S.J., HAGER, W. & HÄNGGI, P. 1999 Hysteretic transition between avalanches and continuous flow in rotated granular systems. *Chaos* **9**, 649–653.

LIU, D. & HENANN, D.L. 2017 Non-local continuum modelling of steady, dense granular heap flows. *J. Fluid Mech.* **831**, 212–227.

LIU, X., ZHOU, S. & SPECHT, E. 2010 Avalanche time of granular flows in rotary kilns. *Chem. Engng Technol.* **33**, 1029–1033.

LUSSO, C., BOUCHUT, F., ERN, A. & MANGENEY, A. 2021 Explicit solutions to a free interface model for the static/flowing transition in thin granular flows. *ESAIM* **55**, S369–S395.

MARTEAU, E. & ANDRADE, J.E. 2018 A model for decoding the life cycle of granular avalanches in a rotating drum. *Acta Geotechnica* **13**, 549–555.

MIDI, G.D.R. 2004 On dense granular flows. *Eur. Phys. J.* E **14**, 341–365.

PAREZ, S., AHARONOV, E. & TOUSSAINT, R. 2016 Unsteady granular flows down an inclined plane. *Phys. Rev.* E **93**, 042902.

PERRIN, H., CLAVAUD, C., WYART, M., METZGER, B. & FORTERRE, Y. 2019 Interparticle friction leads to nonmonotonic flow curves and hysteresis in viscous suspensions. *Phys. Rev.* X **9**, 031027.

RAJCHENBACH, J. 1990 Flow in powders: from discrete avalanches to continuous regime. *Phys. Rev. Lett.* **65**, 2221–2224.

SARNO, L., WANG, Y., TAI, Y.-C., PAPA, M.N., VILLANI, P. & OBERLACK, M. 2022 A well-posed multilayer model for granular avalanches: comparisons with laboratory experiments. *Phys. Fluids* **34**, 113307.

SHERMAN, D.J., ZHANG, P., PELLETIER, J., ELLIS, J., FARRELL, E. & LI, B. 2022 Barchan slipface grainflows: characteristics and kinematics. *Geophys. Res. Lett.* **49**, e2021GL095257.

SILBERT, L., ERTAZ, D., GREST, G.S., HALSEY, T.C., LEVINE, D. & PLIMPTON, S.J. 2001 Granular flow down an inclined plane: Bagnold scaling and rheology. *Phys. Rev.* E **64**, 051302.

TABERLET, N., RICHARD, P., VALANCE, A., LOSERT, W., PASINI, J.M., JENKINS, J.T. & DELANNAY, R. 2003 Superstable granular heap in a thin channel. *Phys. Rev. Lett.* **91**, 264301.

TAI, Y.C. & KUO, C.Y. 2008 A new model of granular flows over general topography with erosion and deposition. *Acta Mechanica* **199**, 71–96.

TAPIA, F., POULIQUEN, O. & GUAZZELLI, E. 2019 Influence of surface roughness on the rheology of immersed and dry frictional spheres. *Phys. Rev. Fluids* **4**, 104302.